UNIVERSIDADE BEIRA INTERIOR

CFD Analysis of Plunging Flat Plates at Low-Reynolds Number

(Versão corrigida após defesa)

Sullivan Benjamim Seixas Gonçalves

Dissertação para obtenção do Grau de Mestre em **Engenharia Aeronáutica** (Ciclo de estudos integrado)

Orientador: Prof. Doutor André Resende Rodrigues da Silva

maio de 2022

Acknowledgments

Firstly, I would like to express my gratitude to my supervisor, Professor André Resende Rodrigues da Silva for his guidance and for providing me with this opportunity. His knowledge coupled with my motivation and enthusiasm allowed me to continuously improve my work.

I am thankful to Professor Jorge Manuel Martins Barata for the opportunity given to work in affiliation with AEROG - Aeronautics and Astronautics Research Center, which gave me access to all the necessary resources and support needed to successfully conclude this dissertation.

I am thankful to have been given the chance to work near my AEROG colleagues, Emanuel Camacho and Francisco Dias, who unceasingly encouraged me to improve my work, with brainstorming, exchange of ideas, through joyful and stressful moments, being there in every step of the way and helping me strive through this work.

I am grateful to my girlfriend, Cristina Primo, and friends with who I was able to share unforgettable moments of my academic and personal life, allowing this journey to be as enriching as possible.

At last, I would like to thank all my family, with special regard to my parents and sister, for believing in me and my skills, supporting me with love, and for being present during all my academic life, through the best and hardest moments, and all the struggles.

Resumo

A análise aerodinâmica em regime transiente passa pelo estudo de objetos sujeitos a oscilações e rotações e, portanto, possui uma forte associação com escoamentos bioinspirados. O principal objetivo desta dissertação é o estudo das características propulsivas de duas placas planas com bordo de fuga reto e afiado para um número de Reynolds, Re de $3,1 \times 10^3$. A frequência reduzida, k, é mantida entre $1,0$ e $5,0$ com uma amplitude adimensional, h, variando entre $0,125$ e $0,500$. O problema é resolvido numericamente usando Dinâmica de Fluidos Computacional (DFC), e os resultados mostram que, contrariamente ao descrito na literatura para perfis alares, o coeficiente de tração médio, $\overline{C_t}$, não aumenta monotonamente com a frequência reduzida, reduzindo em torno de $k = 3,0$ para $h = 0,250$. O mesmo não se verifica para o coeficiente de potência médio, $\overline{C_P}$, aumentando continuamente com a frequência reduzida para todo o domínio de amplitude adimensional estudado. Analisando os contornos de pressão em torno das placas planas, uma zona de baixa pressão foi detetada perto do bordo de fuga, criando um efeito de sucção naquela zona. Ao analisar os parâmetros C_P e C_t ao longo de um período foi evidenciada a influência da recirculação, apresentando um forte impacto no coeficiente de tração. Contudo, os resultados evidenciam a influência de outro fenómeno. A evolução do vórtice de bordo de ataque com k foi analizada, recorrendo a uma distancia normalizada entre o centro do vórtice e a superfície da placa plana, resultando num comportamento similar ao de $\overline{C_t}$ previamente observado. É realizada uma tentativa de relacionar os fenómenos observados com o número de Strouhal, St, identificando-se um carácter previsível dos parâmetros de desempenho no intevalo $0 \leq St \leq 1$. A geometria do bordo de fuga aparenta ter influência nos coeficientes propulsivos obtidos, sendo, na sua generalidade, os valores de $\overline{C_P}$ mais altos e os de $\overline{C_t}$ mais baixos para a placa de bordo de fuga reto, relativamente à placa de bordo de fuga afiado.

Palavras-chave

Bioinspirado, Placa Plana, Asa Batente, DFC, Geometria, *LEV*, Coeficientes Propulsivos

Abstract

Unsteady aerodynamics include the study of flows that pass an object subjected to oscillations, and therefore, has a strong link with bioinspired flows and flapping airfoils. The central objective of the dissertation is to study the propulsive characteristics of two flat plates at a Reynolds number, Re, of 3.1×10^3 with straight and sharp trailing edges. The reduced frequency, k, is kept between 1.0 and 5.0 with a nondimensional amplitude, k, ranging between 0.125 and 0.500. The problem is solved numerically using Computational Fluid Dynamics (CFD), and results show that different from what is typically observed in airfoils, the mean thrust coefficient, $\overline{C_t}$, does not increase monotonically with the reduced frequency, for $h = 0.250$, having a dip around $k = 3.0$. The same is not verified for the mean power coefficient, $\overline{C_P}$, which increases continuously with the reduced frequency for the entire dimensionless amplitude domain studied. Through analysis of pressure contours around the flat plates, a low-pressure zone was detected near the trailing edge, creating a suction effect in that zone. By analyzing the C_P and C_t over one period, the recirculation influence was evidenced, displaying a strong effect on the thrust coefficient parameter. However, results also show the influence of another phenomenon. The LEV's evolution with k was analyzed, via the normalized distance between its center and the surface of the plate, evidencing a behavior similar to the $\overline{C_t}$ one previously observed. An attempt to relate the phenomena with the Strouhal number, St, was made, identifying a predictable feature of the performance parameters for St ranging between 0 and 1. The trailing-edge shape revealed to influence the propulsive coefficients, being the overall $\overline{C_P}$ values higher and the $\overline{C_t}$ lower for the flat plate with a straight trailing edge, when compared to the plate with a sharp one.

Keywords

Bioinspired, Plunging Flat Plate, CFD, Geometry, LEV, Propulsive Coefficients

Index

Acknowledgments iii
Resumo v
Abstract vii
List of Figures xi
List of Tables xiii
Nomenclature xv
List of Acronyms xvii

1 Introduction **1**
1.1 Motivation and Objectives 1
1.2 Outline 3

2 Literature Review **5**
2.1 Problem Configuration 5
2.2 Governing Parameters 5
2.3 Wake Structures 9
2.4 Parameters Dependency 12
2.5 Airfoil Properties 15
2.6 Additional Studies 17

3 Methodology **21**
3.1 Mathematical Models 21
3.1.1 Governing Equations 21
3.1.2 Turbulence Modeling 22
3.1.3 Wall Boundary Conditions 27
3.2 Numerical Methodology 28
3.2.1 Problem Formulation 28
3.2.2 Mesh Configuration 29
3.2.3 Boundary Location 30
3.2.4 Numerical Setup 31
3.3 Numerical Validation 32
3.3.1 Mesh Independence Study 32
3.3.2 Time-Step Independence Study 33
3.3.3 Numerical and Experimental Comparison 33

4 Results and Discussion **39**
4.1 Influence of the Nondimensional Amplitude, h 42
4.2 Influence of the Reduced Frequency, k 42
4.3 Analysis of the aerodynamic phenomena around k = 3.0 43
4.4 Influence of the Strouhal Number, St 46

5 Conclusion **49**

Bibliography **51**

List of Figures

1.1 Effect of Reynolds number on airfoil maximum lift-to-drag ratio. 2

2.1 First theory describing propulsion from flapping wings, Knoller and Betz. 7
2.2 Typical von Kármán vortex street (velocity profile indicates a momentum deficit). 9
2.3 Inverted von Kármán vortex street (velocity profile indicates a momentum surplus). 9
2.4 Transition from typical to inverted von Kármán vortex street. 11
2.5 Deflected vortex street. 11
2.6 Propulsive efficiency at Re = 8.5×10^3 14
2.7 Propulsive efficiency at Re = 1.7×10^4 14
2.8 Propulsive efficiency at Re = 3.4×10^4 14
2.9 Snapshots for four models over one flapping cycle. 16
2.10 Thickness influence on propulsive efficiency. 16
2.11 Qualitative plot showing constant rate heaving motion and its equivalent sinusoidal heaving motion. 18
2.12 Schematic plot of a heaving motion described by a sinusoid followed by a gap, heave is zero during T/fa, fa is a fraction of the sinusoidal time period 18
2.13 Airfoils in tandem configuration 19

3.1 Near-wall treatment approaches. 26
3.2 Subdivisions of the near-wall region. 27
3.3 Flat plates considered. 28
3.4 Flat-plate's trajectory. 29
3.5 Background (left) and flat-plate's (right) meshes. 30
3.6 Parameters evolution for different meshes with U_∞ = 1.0 m/s, A = 28 mm, and f = 1.5 Hz. (^{*1} Divisions of the background mesh) 32
3.7 Parameters evolution for different time steps with U_∞ = 1.0 m/s, A = 28 mm, and f = 1.5 Hz 33
3.8 Comparison between the experimental and numerical trajectories of the flat plate. 34
3.9 Comparison between the experimental and numerical results for Re = 7.8×10^2. 35
3.10 Comparison between the experimental and numerical results for Re = 1.6×10^3. 36
3.11 Comparison between the experimental and numerical results for Re = 3.1×10^3. 37

4.1 Variation of the mean power coefficient, $\overline{C_P}$, with the reduced frequency, k, and the nondimensional amplitude, h 41
4.2 Variation of the mean thrust coefficient, $\overline{C_t}$, with the reduced frequency, k, and the nondimensional amplitude, h 41
4.3 Low-pressure zone near the trailing edges of the flat plates at t/T = 0.50 43
4.4 Power coefficient evolution throughout a period at different k values. 44

4.5 Thrust coefficient evolution throughout a period at different k values.....44
4.6 Variation of the normalized distance between the LEV's center and the plates' surface, y_v, with k.....45
4.7 Variation of the mean power coefficient, $\overline{C_P}$, with kh.....47
4.8 Variation of the mean thrust coefficient, $\overline{C_t}$, with kh.....47
4.9 Maximum effective angle of attack evolution for different k values.....48

List of Tables

3.1 SST k – ω turbulence model constants. 25

4.1 Mean power and thrust coefficients values of the simulated cases. 40

Nomenclature

A	Plunging amplitude	m
A_α	Pitching amplitude	rad
c	Aerodynamic chord	m
C_d	Drag coefficient	–
C_l	Lift coefficient	–
C_m	Moment coefficient	–
C_P	Required power coefficient	–
C_t	Thrust coefficient	–
D	Cross-diffusion term	–
D_ω^+	Positive portion of the cross-diffusion term	–
f	Plunging frequency	s^{-1}
$\widetilde{G}, G$	Generation term	–
h	Nondimensional amplitude	–
k	Reduced frequency, Turbulent kinetic energy	–,m^2/s^2
L	Inlet length	m
$\vec{r}$	Displacement vector from the upstream cell centroid to the face centroids	–
Re	Reynolds number	–
S	User-defined source term, Strain Magnitude	–,s^{-1}
St	Strouhal number	–
t	Time, Thickness	s,m
T	Plunging period	s
u	Velocity	m/s
U_∞	Free-stream speed	m/s
W	Wake length	m
x	Spatial coordinate	m
y	Airfoil's vertical coordinate	m
y_p	Distance from the cell centroid to the nearest wall	m
y_v	Normalized distance between the LEV's center and the flat-plate surface	–
y^+	Dimensionless distance from the cell centroid to the nearest wall	–
Y	Distance to the closest surface, Dissipation term	m,–
$\dot{y}$	Airfoil's vertical velocity	m/s
Δt	Time interval	s
$\bar{\cdot}$	Mean value	–

Greek symbols

α	Angle of attack	rad
$\dot{\alpha}$	Angle of attack rate	rad/s
Γ	Effective diffusity term	–
δ_{ij}	Kronecker delta function	–
ζ	Blockage ratio	–
η	Propulsive efficiency	–
μ	Dynamic viscosity	$Pa \cdot s$
μ_t	Turbulent viscosity	$Pa \cdot s$
ρ	Density	kg/m^3
σ	Turbulent Prandtl number	–
τ_ω	Wall shear stress	Pa
ϕ	Phase angle between plunging and pitching, Cell-centered value	rad,–
$\nabla\phi$	Gradient in the upstream cell	–
ω	Specific dissipation rate	s^{-1}

Subscripts

eff	Effective
max	Maximum
f	Face value
i, j	Cartesian directions
k	Turbulent kinetic energy
w	Wall
ω	Specific dissipation rate
τ	Friction
t	Turbulent

Superscripts

$'$	Fluctuation

List of Acronyms

2D	Two-Dimensional
3D	Three-Dimensional
CFD	Computational Fluid Dynamics
DARPA	Defense Advanced Research Projects Agency
HALE	High-Altitude Long-Endurance
LEV	Leading-Edge Vortex
MAV	Micro-Air Vehicle
NACA	National Advisory Committee for Aeronautics
NAV	Nano-Air Vehicle
PRESTO	PREssure STaggering Option
RANS	Reynolds Averaged Navier-Stokes
SST	Shear-Stress Transport
TEV	Trailing-Edge Vortex
TE	Trailing Edge
UDF	User-Defined Function

Chapter 1

Introduction

In the first chapter, the motivation behind this work and the objectives established are described, followed by the outline section, where the structure and organization of the dissertation are explained.

1.1 Motivation and Objectives

Historically, humankind has felt the urge to fly, inspired by animals like birds and insects. As a result, the scientific community aimed their resources to research and analyze these animals, beginning with the understanding and study of what were the mechanisms that enabled flight, as well as differentiating the ones responsible for the production of lift and thrust.

A rise in interest for some military and civil purposes, using small flying vehicles, promoted the development of Micro Air Vehicle (MAV) and Nano Air Vehicle (NAV). These first ones are described by Petricca et al. [1] as "extremely small and ultra-lightweight air vehicle systems", which based on the definition by the Defense Advanced Research Projects Agency (DARPA) are vehicles that present a maximum dimension of 15cm, and can display a variety of configurations.

With these improvements, missions under dangerous conditions or of hard access to humans had a great increase in their effectiveness, safety, and success rate. Simultaneously, with the development of MAVs and NAVs, the interest of the scientific community increased. Thanks to the performance and mechanisms of air vehicles with such small dimensions, a more direct comparison with their biological equivalents was made, due to the similarity between their flight conditions.

Although some vehicle configurations, such as rotary and fixed wings, are very well-known and their efficiency verified, in some conditions they revealed to be not optimal for the mission. In some cases, due to low Reynolds numbers and unsteady effects, new alternative configurations must be investigated.

Subsequently, to improve the efficiency of the flying mechanism, further investigation was directed to develop a mechanism responsible for the production of thrust and lift. This led to the creation of the flapping mechanism which was heavily inspired by nature mechanisms. Nevertheless, the effort of understanding this flapping mechanism only increased at the end

of the twentieth century.

The growing understanding of this flying mechanism aroused new interests in the scientific community when possible applications of this technology were identified. One of these, as proposed by Shrestha et al. [2] is Martian exploration as an alternative to the ground vehicles used nowadays. The most usual configuration would be a rotary wing, which allows to take off and land vertically on harsh terrain, offers more stability, range, and field of view when compared to a ground vehicle. Although, even with lower gravity force (about 38% of Earth's gravity force), the Martian atmosphere presents a set of conditions that hamper the flight with this common mechanism. These conditions result in a low Reynolds number environment, at which the use of a flapping mechanism is beneficial.

Despite displaying great performance at higher Reynolds numbers where the flow is mainly steady, the typical airfoil loses that feature with the decrease of this parameter. In fact, as shown in Figure 1.1, the flat plate becomes more efficient at low-Reynolds numbers, surpassing conventional airfoils.

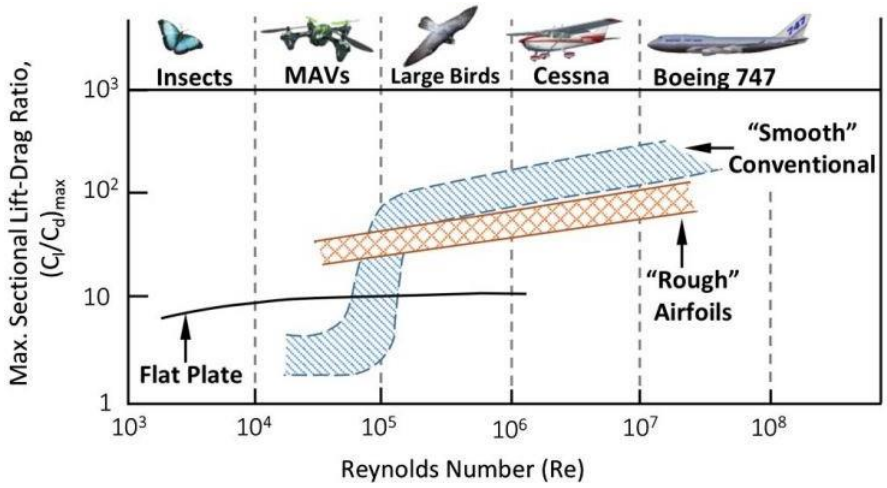

Figure 1.1: Effect of Reynolds number on airfoil maximum lift-to-drag ratio [3].

This dissertation is motivated by the interest in understanding the flapping wing configuration and the possible improvements that may come with it. There is a need to replicate the natural flight mechanism that has been improving through natural evolution, to reach the maximum efficacy and performance in any condition or situation.

The two-dimensional (2D) plunging motion of two different flat plates are studied in this dissertation, using Computational Fluid Dynamics (CFD) and validating the simulation with Marques [4] experimental studies. These are characterized by a thickness of 5 mm, having one of them a sharp leading edge, and the other, featuring sharp leading and trailing edges.

The numerical computation of these flat plates undergoing a plunging motion serves the purpose of trying to better understand the influence of different trailing edge shapes on the

wake structure formation and propulsive efficiency as well as thrust and lift production. In addition, understanding the dependence between the variables that govern the flat-plates' motion, such as amplitude, frequency, effective angle of attack and flow velocity is a clear objective. For the parameters enunciated above, dimensionless equivalents will be used to describe the conditions of the plunging motion, being these the nondimensional amplitude, the reduced frequency, and the Reynolds and Strouhal numbers.

1.2 Outline

The dissertation is divided into five chapters: Introduction, Literature Review, Methodology, Results and Discussion, and Conclusion.

The Introduction chapter focused on the motivation behind this dissertation and its main objectives. Next, the Literature Review chapter includes bioinspired works, which give the theoretical background and advances required to develop this work. The third chapter starts by describing the mathematical models used for simulations, followed by the numerical methodology, where the problem formulation is exhibited and the numerical procedure is explained. The Results and Discussion chapter is where the numerical results are presented, displaying all the simulated cases and showing the relations between the performance parameters, the kinematic parameters, and phenomena observed. The final chapter presents the conclusions obtained from this study and introduces questions and ideas for possible future works to improve the investigation of the flapping airfoil problem.

Chapter 2

Literature Review

In the following chapter, the literature review is presented and complemented by the research conducted by other authors, being segmented in varied topics, in order to better understand the theory behind the phenomena in study.

2.1 Problem Configuration

The scientific community started the research on understanding of the flapping motion in the 20th century, basing it on aero/hydrodynamic performance, energy harvesting, flow structures, and bionics. With it, different methodologies and approaches to the problem commenced to be set, resulting in the creation of two main configurations: zoological and simplified configurations.

The works and studies that follow a zoological configuration base themselves on a close to nature approach, studying animals, the flow conditions they fly in, and the way they use and adapt their natural structures in different conditions. On the other hand, when following the simplified configuration, the works are mainly bidimensional or tridimensional simulations and experiments, based on simple airfoils or flat plates subjected to controlled movements and flow conditions, with the objective of calculating and predicting aerodynamic forces and propulsive efficiency.

2.2 Governing Parameters

Through observations of animals and the locomotion mechanisms used by many, such as insects, birds, or fishes, the similarity between them becomes evident. The pitching and plunging motions alone and the flapping motion, being the combination of the two first motions, reveal themselves as mechanisms that must be investigated to understand the aerodynamic conditions that allow an effective flight with them.

Although, despite flying using flapping-wing mechanisms, different animals such as birds and insects adopt different flapping strategies in completely different conditions. For instance, birds fly in a relatively high-Reynolds number environment while insects fly in ultra-low-Reynolds number environments.

The aerodynamic conditions previously mentioned are intrinsically related to the flow properties, and airfoil movement, so the use of several governing parameters is crucial to better

understand this mechanism and the phenomenon associated with them. According to Wu et al. [5], these parameters can be divided into four categories:

- Environmental parameter, describing the fluid properties;
- Geometric parameter, describing the shape of foils;
- Kinematic parameter, describing the motion of foils;
- Performance parameter, describing propulsion or energy harvesting performance of foils.

Starting with the Reynolds number, this environmental parameter represents the ratio of inertial to viscous forces and it is used to categorize the fluid flow, being defined as

$$Re = \frac{\rho U_\infty c}{\mu} \tag{2.1}$$

where ρ is the fluid density, U_∞ is the inlet speed, c is the airfoil chord and μ is the dynamic viscosity of the fluid. However, this parameter does not take into account the oscillatory movement of bodies in the flow.

One of the parameters regarding the airfoil movement is the reduced frequency. This dimensionless number is mainly used for cases of unsteady aerodynamics and relates the flapping velocity with the incoming flow velocity, being defined as

$$k = \frac{2\pi f c}{U_\infty} \tag{2.2}$$

where f is the airfoil motion's frequency. Usually, k comes together with the nondimensional amplitude parameter that is defined as

$$h = \frac{A}{c} \tag{2.3}$$

where A is the airfoil motion's amplitude. With the flow being characterized by a periodic motion of an airfoil, the Strouhal number can be defined as a parameter that represents the ratio of inertial forces due to the oscillations of the airfoil to inertial forces due to convective acceleration of the flow field. The Strouhal number parameter can be defined as

$$St = \frac{fW}{U_\infty} \tag{2.4}$$

where W is the wake length that is equal to two times the airfoil plunging amplitude ($W = 2A$). In this parameter the frequency f considered is the airfoil's motion frequency instead of the vortex shedding frequency. Having the Strouhal number, k and h parameters defined,

we can show that

$$kh = \pi St \tag{2.5}$$

In the early twentieth century, Knoller [6] and Betz [7], by focusing their studies on the flapping wing mechanism, introduced the idea of an effective angle of attack created by the plunging motion of an airfoil, being defined by

$$\alpha_{eff} = \arctan \frac{-\dot{y}(t)}{U_\infty} + \alpha(t) \tag{2.6}$$

where $\alpha(t)$ is the angle of attack, given by

$$\alpha(t) = \alpha_0 + A_\alpha \sin(2\pi ft + \phi) \tag{2.7}$$

where A_α is the pitching amplitude, f the frequency and ϕ the phase angle between plunging and pitching.

The effective angle of attack would change over time, creating an oscillatory aerodynamic force normal to the relative velocity which could be decomposed in lift and thrust forces. The plunging motion resulted in positive and negative lift forces and positive thrust forces, as demonstrated in Figure 2.1.

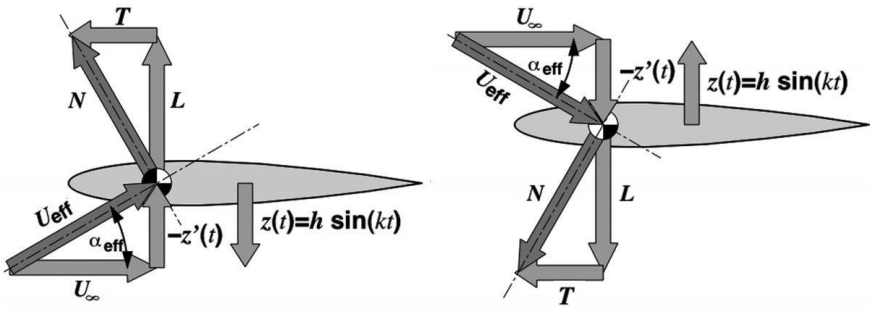

(a) Downward plunging motion. (b) Upward plunging motion.

Figure 2.1: First theory describing propulsion from flapping wings, Knoller [6] and Betz [7].

However, this study did not take into account the vorticity shed of the airfoil, which was later proved to be a signature of the thrust and lift production mechanisms. As stated by Helmholtz's second and Kelvin's theorems, for potential flow, the flow circulation must be constant in time, thus, there must be an equivalent opposite circulation in the wake generated by the airfoil. Nonetheless, as recognized by Platzer et al. [8], if the Reynolds number is sufficiently large and the angle of attack is kept small, inviscid flow analysis methods present acceptable results.

Unlike in a pure plunge motion where the aerodynamic forces are generated due to the effective angle of attack created by the vertical movement of the airfoil, in a pure pitching motion those forces are created by the angle of attack of the airfoil itself.

With the study of the flapping wing mechanism, comes the need to understand its propulsive nature, and the resulting thrust production and propulsive efficiency. For that purpose, the performance parameters, such as thrust and power coefficients, are used to better understand and describe the resulting forces and propulsive efficiency. The mean thrust and power coefficients, $\overline{C_t}$ and $\overline{C_P}$, respectively, are defined by the equations 2.8 and 2.9

$$\overline{C_t} = -\frac{1}{\Delta t}\int_{t}^{t+\Delta t} C_d \, dt \tag{2.8}$$

$$\overline{C_P} = -\frac{1}{\Delta t}\int_{t}^{t+\Delta t} \frac{\dot{y}C_l + \dot{\alpha}C_m}{U_\infty} \, dt \tag{2.9}$$

where C_t is the thrust coefficient, C_d is the drag coefficient, C_P is the power coefficient, C_l is the lift coefficient and C_m is the moment coefficient.

The propulsive efficiency, given by the ratio between generated and supplied power, is defined as

$$\eta = \frac{\overline{C_t}}{C_P} \tag{2.10}$$

It should be emphasized that, despite the C_t parameter being called thrust coefficient, it equals the propulsive power coefficient, so the propulsive efficiency is given by the ratio between two power coefficients.

In 1936, Garrick [9] analyzed both the pure plunge and the pure pitch oscillation of a flat plate in potential flow, which does not take into account the viscous effects and only represents small motion amplitudes. The author observed that pure pitch oscillations start to generate thrust only after at relatively high-frequency values. Later, Koochesfahani [10] provided accurate flow visualizations and measurements for this motion, concluding that it is not a viable option for thrust generation.

In 2017, Andersen et al. [11] demonstrated the comparability between the pitching and the plunging motion of a 2D airfoil. Through numerical simulation and further experimental validation, the similarity between the two different motions was proved by comparing the wakes produced.

The same year, Moubogha et al. [12] studied the forces generated by the pitching motion of a flat plate in a water channel at $Re = 2.0 \times 10^3$ based on the plate chord c, through experimental and numerical approaches. An acceptable comparison between the results of the two approaches was established by selecting a quasi-two-dimensional configuration to minimize the three-dimensional effects of the experimental work. Moubogha et al., keeping a constant plate motion's amplitude, determined the oscillation frequency above which the

velocity profile in the wake presents a velocity excess, being a sign of thrust production, and the wake produced presents a reverse von Kármán street structure. However, despite the use of a quasi-two-dimensional configuration, the finite-width effects may influence the thrust production through flapping and must not be neglected.

2.3 Wake Structures

The vorticity shed of the airfoil was taken into account by Kármán and Burgers work [13], where they explained the thrust generation mechanism using the vorticity shed of the airfoil on the downstream side and the orientation of the wake vortices. By studying the flow interaction with bluff bodies and flat plates or airfoils, at low Reynolds numbers in pure plunging, pitching or both motions combined, a clear difference between the wakes produced was visualized.

The wake generated by the interaction with the bluff bodies is a wake associated with drag production, designated as a von Kármán vortex street. This type of wake is characterized by a momentum deficit, comparatively to the upstream flow. The von Kármán vortex street is shown in Figure 2.2.

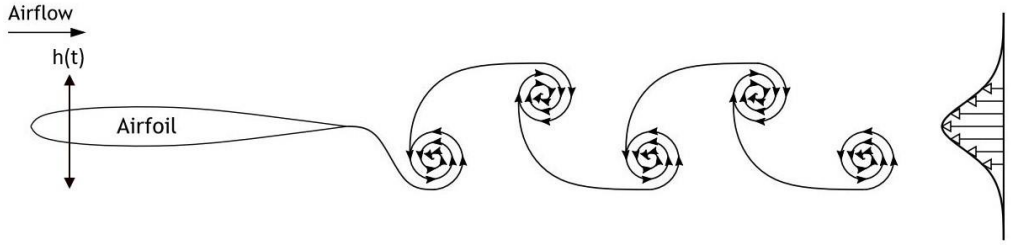

Figure 2.2: Typical von Kármán vortex street (velocity profile indicates a momentum deficit) [14].

On the other hand, the wakes generated by the interaction with flat plates or airfoils, undergoing plunging or pitching motions, sometimes give rise to a momentum surplus in the wake, comparatively to the upstream flow. This wake structure was named as an inverted von Kármán vortex street and designated as a thrust production wake, being that thrust explained by Newton's third law of motion. Figure 2.3 represents this wake structure.

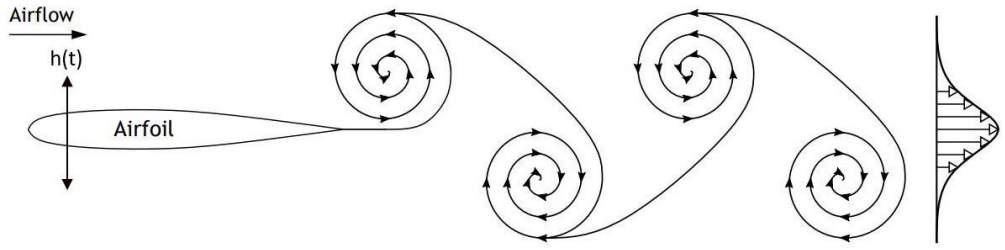

Figure 2.3: Inverted von Kármán vortex street (velocity profile indicates a momentum surplus) [14].

With the continuous work directed to understand the type of wake structure, it was found that the vortex structure formation varies under different conditions. This variation depends on kinematic parameters, such as the motion amplitude and frequency, which also affect the forces generated by the flapping wing mechanism.

In 1988, Freymuth [15] visualized and identified the vortical structures behind plunging and pitching airfoils, being these inverted von Kármán vortex streets. It was concluded that these wake structures were created by the pure plunging or pitching motions, at sufficiently low angles attack, α, high reduced frequencies, k, and small plunge amplitude, A, for a given frequency to avoid severe separation from the leading edge of the airfoil.

The following year, Koochesfahani [10] studied the vortical flow patterns in the wake of a NACA0012 airfoil pitching at small amplitudes in a low-speed water channel. With his experiment, it was shown that the structure of the wake could be controlled by manipulating the frequency, amplitude values, and shape of the oscillation waveform. Koochesfahani added that this last parameter alone has a strong effect on the wake structures and the vortex-vortex interactions.

In 1999, Lai and Platzer [16] analyzed the wake structures created by the plunging motion of a NACA0012 airfoil with the dimensionless parameter kh. It was concluded that the vortex patterns of the airfoil change from drag-producing, for kh values lower than 0.2, to thrust-producing wakes, for kh values above 0.4. For the kh values between 0.2 and 0.4, the wake structure transitions through a neutral wake.

Similarly, flapping airfoils have been studied in other works, such as Lewin and Haj-Hariri [17] or Godoy-Diana et al. [18], where the different wake structures and the transition between the drag-producing and the thrust-producing wakes are analyzed. Young and Lai [19], analyzing a NACA0012 airfoil in flapping motion, visualized flow separation upstream of the trailing edge on both sides of the airfoil, acting as a blunt-edged body. This effect resulted in vortices being shed alternately from either side of the trailing edge with a known vortex shedding frequency that varies with the Reynolds number. This type of shedding is referred to as natural shedding, and the shedding induced by the airfoil motion is referred to as forced shedding. They concluded that the interaction between the blunt-edged body effect and the airfoil motion led to the transition from the drag-producing wake to the thrust-producing wake, as shown in Figure 2.4.

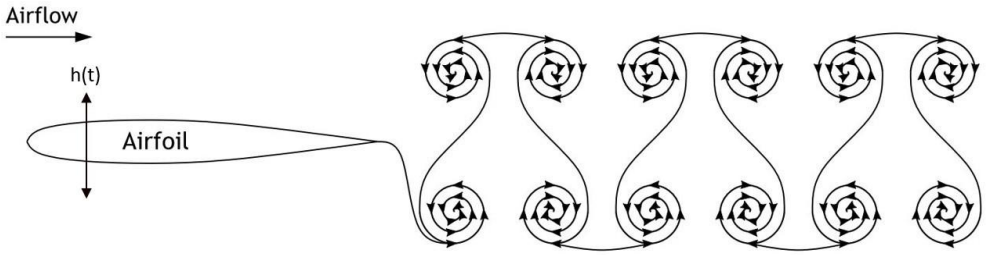

Figure 2.4: Transition from typical to inverted von Kármán vortex street [14].

Jones et al. [20], through experimental and numerical methods, studied the wake structure formation, visualizing an asymmetrical vortex shedding. According to the results obtained experimentally and numerically, the wake structures visualized at Strouhal numbers greater than 1, were nonsymmetric, dual-mode, deflected wake patterns. It was concluded that this wake structure formation was essentially an inviscid effect due to the closeness of the shed vortices and observed that the deflected wake could switch from deflected up or down with relatively small disturbances.

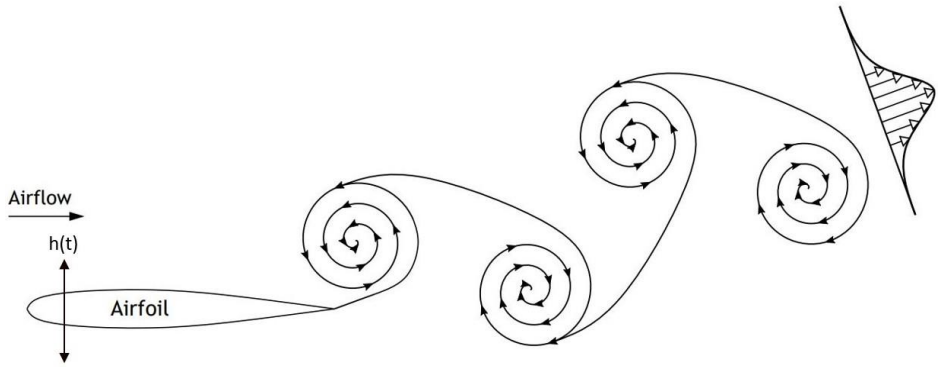

Figure 2.5: Deflected vortex street [14].

As shown above, the flapping wing mechanism produces wake structures composed of alternating vortices responsible for the thrust or drag production. Also, in some circumstances, vorticity may appear near the leading edge. The leading-edge vortex (LEV) issues from intense adverse pressure gradients, being intrinsically related to kinematic and geometric parameters, and its benefits on the thrust production and propulsive efficiency still require additional investigation.

Li and Lu [21] numerically analyzed the vortex dynamics of three-dimensional (3D) flapping plates to study the generated forces and power. The study allowed them to conclude that the vortical structures close to the surface of the plate greatly influence the resulting forces and power. Furthermore, they visualized that, for each vortical structure, the vortical impulse is almost conserved and the kinetic energy progressively decays.

Rodrigues et al. [22] experimentally studied the wake structures of a NACA0012 airfoil at Reynolds number of 1.5×10^3 experiencing a periodic asymmetrical motion. It was observed that, under these conditions, the airfoil would produce, simultaneously, thrust and lift. Moreover, they noted that the LEV formation and its convection allow a possible required

power reduction and lift production increasement, due to the presence of a low-pressure zone. The authors further added that it's never recommended an LEV passing the maximum thickness position when trying to increase thrust production.

2.4 Parameters Dependency

To better predict and control the vortices shedding behavior and the wake structure formations, the studies of the flapping mechanism had to focus on the understanding of the parameters' impact and dependency on each other. Efforts in that direction have great importance allowing the optimization of the propulsive efficiency and thrust coefficients.

With that purpose, in 2003, Lewin and Hariri [23] presented a numerical model for two-dimensional flow around a rigid foil at zero mean angle of attack, subjected to sinusoidal plunging motions, to analyze the flow characteristics and power coefficients resulting from the airfoil motion. The study was executed considering an incompressible viscous flow with constant horizontal free-stream velocity. By maintaining a constant Reynolds number of 5.0×10^2 and varying the frequency and plunging speed values, they visualized different wake patterns.

Lewin and Hariri concluded that these patterns are greatly correlated with the LEV behavior and its possible interaction with the trailing-edge vortex (TEV), being the reduced frequency, k, being responsible for the configuration of the LEV.

For low k values, the LEV separates and advects downstream, usually interacting with the TEV. As increasing it, the LEV separation is delayed in each movement cycle, which causes it to stretch and dissipate by the following LEV formed. For high kh the LEV enters a transition region where the wake, irregularly, sheds or dissipates. Finally, for high k and kh values, the LEV can circle the leading edge to the other side of the foil and advect downstream either in the boundary layer of that side or the free stream.

The results display the importance of the timing of the LEV separation on the thrust production and efficiency of the plunging motion. When the LEV remains attached as long as the stroke duration, leading to positive reinforcement of the TEV, the efficiency reflects a significant gain. However, when the LEV interacts negatively with the TEV, the efficiency considerably reduces.

Later, Lua et al. [24] adapted the numerical study completed by Lewin and Hariri [23], carrying out an experimental study of the wake-structure formation of a plunging 2D elliptic airfoil. Although having changed the cross-section of the airfoil and raised the Reynolds number to a constant value of about 1.0×10^3, the obtained results remained mainly similar to Lewin and Hariri's conclusions. Adding to those, Lua et al. concluded that the wake structure produced also depends on the nondimensional plunging amplitude. When maintaining the reduced frequency constant, the plunging velocity controls the amplitude of the motion,

being the LEVs and TEVs stronger with the increasing plunging velocity. However, with that increase, the LEVs gain a tendency to shed before the end of the stroke.

In 2010, Baik et al. [25] studied, experimentally, an oscillating airfoil at a Reynolds number of 1.0×10^4 undergoing a pitching and plunging motion and a pure sinusoidal plunging motion to analyze the influence of the Strouhal number, St, reduced frequency, k, and dimensionless amplitude, h. The results showed dependency between the LEVs formation phase and the reduced frequency when maintaining a fixed Strouhal number and nondimensional amplitude, being the LEV formation delayed for higher reduced frequencies, k. Baik et al. also concluded that the circulation of LEV is not ruled by St, k, and h, being controlled by the Re and the effective angle of attack. Additionally, it was demonstrated that the velocity profile normal to the airfoil is similar when maintaining an effective angle of attack and reduce frequency, independently of the other parameters' variation.

Panah and Buchholz [26] analyzed two-dimensionally the LEVs and TEVs production originated by a flat plate subjected to a sinusoidal plunging motion at a Reynolds number of 1.0×10^4. According to the results, the authors revealed the strong dependency between the LEV and TEV shedding patterns and the Strouhal number. Moreover, they showed that the trajectory of the LEV and its following interaction with the TEV is influenced by the plunging amplitude.

A few years later, Panah and Buchholz [27] studied experimentally the patterns, and the evolution of LEV and TEV structures shed produced by a flat plate undergoing the same conditions as their previous work [26]. It resulted in the construction of a wake classification scheme based on the nature and timing of interactions between LEVs and TEVs.

Comparing their results with the experimental and numerical results obtained by Lewin and Hariri [23] and Lua et al. [24], respectively, they concluded that, despite the different order of magnitude of the studied Reynolds numbers, a great part of the results presented similarities. However, on most of the wakes structures of Lua et al.'s results with $h < 0.4$, the LEV merges with the TEV created in the following stroke, behavior that only was observed on this work for $0.52 < h < 1.18$ with an equal St value. This difference implies that the Reynolds number and the cross-section geometry of the airfoil have a role in the vortex shedding patterns.

In order to improve the energy harvesting performance of the flapping wing mechanism, in 2017, Kim et al. [28] studied experimentally the energy harvesting performance and the resulting wake structures of many hydrofoils undergoing pitching and plunging motions in a free-surface water flume. The experiments were executed mainly using hydrofoils presenting an elliptical or rectangular cross-section, with a 10cm chord and 1cm thickness, at a $Re = 5.0 \times 10^4$, based on the chord length and free-stream speed. Rather than analyze the total propulsive efficiency of the flapping motion, the propulsive efficiency of the individual pitching and plunging motions were analyzed. According to the results, Kim et al. concluded, at optimal pitching amplitude, that the plunging motion contribution to the propulsive ef-

ficiency increases with the reduced frequency. Though, in a pitching motion, that gain decreases with the reduced frequency on account of the delayed LEV formation at high reduced frequencies. Relatively to the aspect ratio of the foil, its increment affects linearly the efficiency in a plunging motion, having roughly no effect on a pitching motion.

Few years later, two numerical parametric studies of a plunging NACA0012 airfoil at different Reynolds numbers ($Re = 8.5 \times 10^3$, 1.7×10^4, 3.4×10^4) were presented by Camacho et al. [29] [30], being the first one mainly focused on the influence of the Reynolds number, reduced frequency, and nondimensional amplitude, and the following one studying the influence of the angle of attack. To analyze the propulsive performance, the authors used the lift, thrust, power coefficients, and propulsive efficiency. By comparing the power coefficient isolines to the hyperbolas of equal Strouhal number, it was concluded that this last parameter is interesting by allowing correlations with the aerodynamic performance, however not enough to characterize the fluid flow. It was observed that for lower Reynolds numbers, high reduced frequency and lower amplitudes are favored, allowing a higher propulsion efficiency, meanwhile, for higher Reynolds Numbers, the opposite would occur.

On the second work, maintaining a constant mean angle of attack during the oscillatory motion of the airfoil, they concluded that the efficiency curves would translate vertically with the increasing Reynolds number but would display the opposite, quadratically, with the angle of attack. Furthermore, it was determined that the power coefficient is kept constant with the variation of the angle of attack. The results are displayed in Figures 2.6, 2.7, and 2.8.

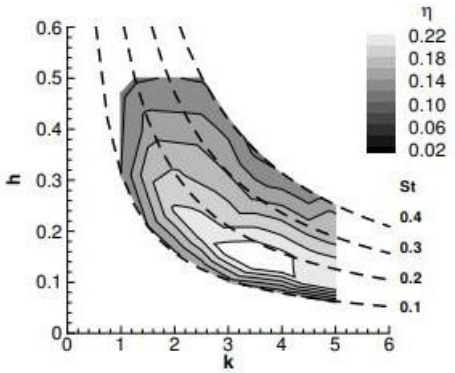

Figure 2.6: Propulsive efficiency at $Re = 8.5 \times 10^3$ [30].

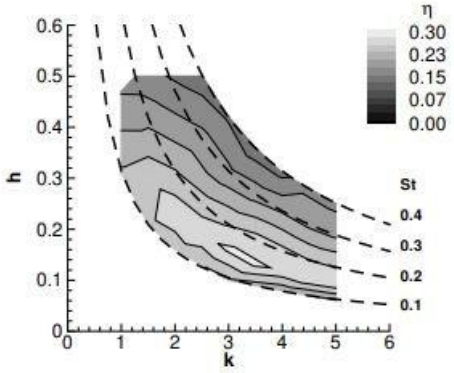

Figure 2.7: Propulsive efficiency at $Re = 1.7 \times 10^4$ [30].

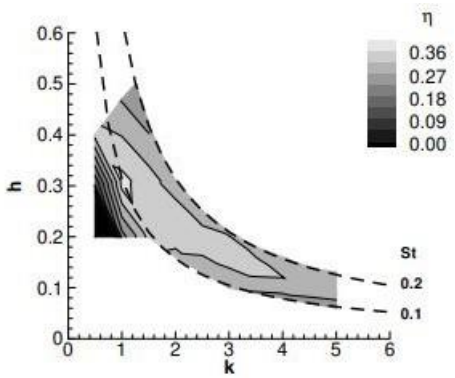

Figure 2.8: Propulsive efficiency at $Re = 3.4 \times 10^4$ [30].

2.5 Airfoil Properties

In order to better understand nature phenomena, Ellington et al. [31] followed by Liu et al. [32] studied experimentally and numerically, respectively, the insect flight to understand the occurring aerodynamic conditions of the flight. Through the experimental work, it was found that an intense LEV was formed on the downstroke resulting in high-lift forces and that the speed of the formed vortex in the spanwise direction is comparable to the flapping speed. On the other hand, the CFD modeling approach allowed to see that the LEV remains attached to the leading edge of the wing during the flapping motion, causing a lower pressure region, being shed after due to quick pronation or supination at the end of it. Additionally, it was demonstrated that lift production occurs mainly during the latter half of the upstroke motion and the entire downstroke of the plunging motion.

After these works, the importance of the pronation and supination movements on the improvement of the propulsive efficiency by controlling the timing of the LEV shed was highlighted and, consequently, more studies focused on understanding and replicating this process were executed. To achieve that, the implementation of flexibility on airfoils was crucial.

In 2006, Pederzani and Hariri [33] studied numerically the influence of flexibility in the propulsion efficiency, for 2D unsteady viscous flow around different airfoils. Maintaining the Reynolds number at 5.0×10^2, typical of insect flight, and varying the kh values between 0.8 and 1.0, three airfoil configurations were tested. The first one was a rigid airfoil to be used as a reference, the second one was a flexible airfoil with a fixed trailing edge, and the third one was a flexible airfoil with a moving trailing edge. The flexible configurations proved to have greater efficiency than the rigid one, being the last configuration the one that presented the best efficiency of the three. Additionally, the density of the airfoils proved to be crucial in determining efficiency and power. By increasing the density, less power would be generated but, proportionately, even less input power would be required, resulting in a gain in efficiency.

Similarly, the following year, Heathcote and Gursul [34] studied experimentally chordwise-flexible airfoils undergoing plunging motions with constant amplitude and Reynolds number varying between 9.0×10^3 and 2.7×10^4. They found out that a certain level of flexibility enhances substantially the thrust coefficient and propulsive efficiency. Furthermore, in an analogy with oscillating rigid airfoils, it was concluded that the aerodynamic performance is dependent on the Strouhal number and pitch phase angle.

Liu et al. [35] modeled computationally four 2D non-passive flexible flapping wings models in single and twin configurations at a Reynolds number of 1.0×10^6. The models are displayed in Figure 2.9. They proved that the angle of attack has an influence on power efficiency and showed that the deformation due to flexibility results in an increase of this parameter. It was remarked, at an effective angle of attack of 10°, that the propulsive efficiency increases 7.68% when the flexibility is introduced. However, at an effective angle of attack of 0°, a drastic

enhancement of power efficiency of about six times was detected, in comparison with the rigid airfoil. Moreover, the twin airfoil configuration used by Liu et al. shows an increment in efficiency when compared to the single airfoil configuration.

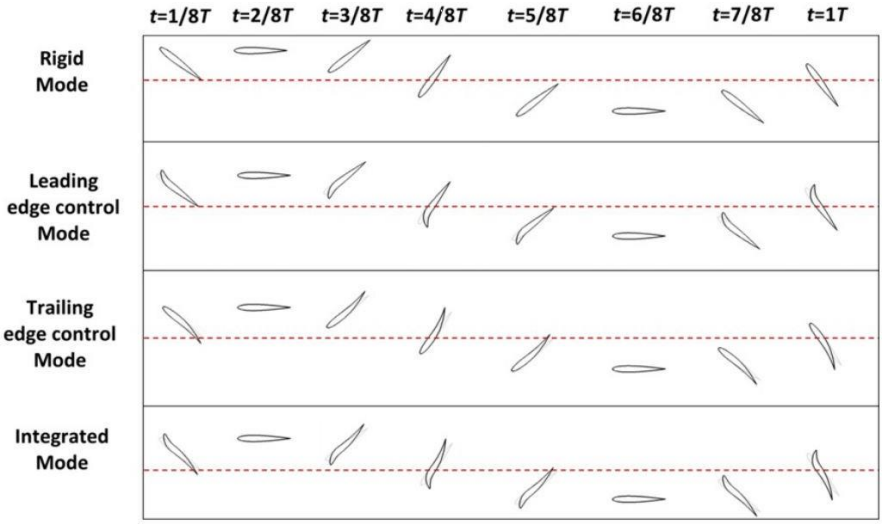

Figure 2.9: Snapshots for four models over one flapping cycle [35].

On the same year, Dewey et al. [36] presented experimental results of an oscillating airfoil with flexibility and concluded that operating at resonance frequency is not a guarantee of efficient locomotion. Instead, that guarantee is given at a frequency that yields a Strouhal number in the range of $0.25 < St < 0.35$, which was claimed by Triantafyllou et al. [37] as being the range to achieve optimal propulsion.

Jones and Platzer [38] executed a 2D numerical computation using different wing configurations to calculate the propulsion and power extraction of the mechanism. By using different NACA airfoils, as shown in Figure 2.10, it was concluded that the variation of the thickness had almost no influence on the propulsive efficiency for the spectrum of reduced frequencies and nondimensional amplitude of this work ($h = 0.1 - 0.4$; $k = 0.01 - 10$).

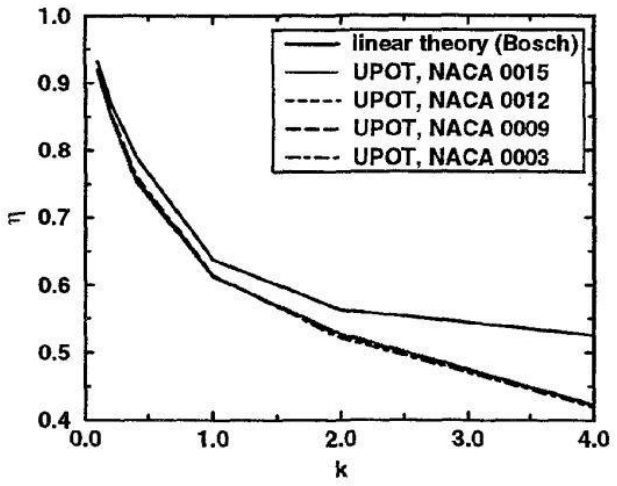

Figure 2.10: Thickness influence on propulsive efficiency [38].

In 2012, Yu et al. [39] dedicated their work to the investigation of the airfoil thickness effect on thrust production of NACA airfoils undergoing a plunging motion. The numerical study was executed maintaining the Reynolds number ($Re = 1.2 \times 10^3$), the Strouhal number ($St = 0.45$), and the reduced frequency ($k = 3.5$) constants, and by varying the thickness of the airfoil between 4% and 20% of the chord length. The authors concluded that for thin plunging airfoils, the viscous forces turned to be thrust-producing, representing around 20% of the total thrust produced by a NACA0004 airfoil in these conditions. However, for thicker airfoils, the opposite occurs, being pressure forces responsible for the majority of thrust production and viscous forces having almost no effect, mostly resulting in drag production.

The following year, Yu et al. [40] studied numerically the influence of airfoil thickness and kinematics effects on the propulsion resulting of an airfoil undergoing flapping motion. They found that, at a low Strouhal number ($St = 0.3$), thin airfoils would favor better aerodynamic performance, independently of the reduced frequency. Though, at higher Strouhal number ($St = 0.45$), that performance turned to be more dependent on the reduced frequency. Additionally, it was concluded that, at a constant Reynolds number, thin airfoils present a greater aerodynamic performance, being thrust production not influenced to a great extent by the variation of the Reynolds number.

Recently, Marques [4] analyzed experimentally the influence of the thickness and trailing-edge shape on an oscillatory flapping flat plate. For the plates with a straight trailing edge, the results showed that the thicker flat plate would present a drag-producing wake meanwhile the thinner one would present signs of a thrust-producing wake. Meanwhile, the flat plate with a sharp trailing edge presented a thrust-producing wake. Moreover, the thickness variation resulted in alterations to the LEV behavior, being its formation favored with the thinner flat plate.

2.6 Additional Studies

The understanding of the flapping wing mechanism and the flapping airfoil have gain importance among the scientific community, having the studies around this subject vastly increased these latest years. To be able to predict and control the outcome of this mechanism, the aerodynamic phenomena and the properties of the airfoil itself were widely investigated through both experimental and numerical methods. Several works took place, directed to analyze the influence of the governing parameters previously stated in this chapter, the influence of physical properties of the airfoil, and the impact of different airfoil configurations.

The hypothesis that the force response of a two-dimensional and three-dimensional flapping wing mechanism have similar dependencies on some governing parameters was investigated by von Ellenrieder et al. [41]. The experimental study focuses on the variation of the Strouhal number, the plunge/pitch amplitude, and pitch angle, showing how these parameters affect the wake structure. Additionally, a 3D model representation was elaborated from the image

sequences obtained with the experiment.

Sarkar and Venkatraman [42] analyzed numerically a plunging airfoil undergoing three different motions, which are asymmetric sinusoidal plunging motion, constant rate plunging oscillations, as shown in Figure 2.11, and sinusoidal motions with a latent time gap, as shown in Figure 2.12. It was shown that for the same plunge velocity and reduced frequency, an airfoil subjected to the first type of motion presents better propulsive efficiency than one subjected to a pure harmonic motion. In terms of wake structure, the asymmetric sinusoidal cases presented a more deflected wake structure when compared to the pure sinusoidal cases.

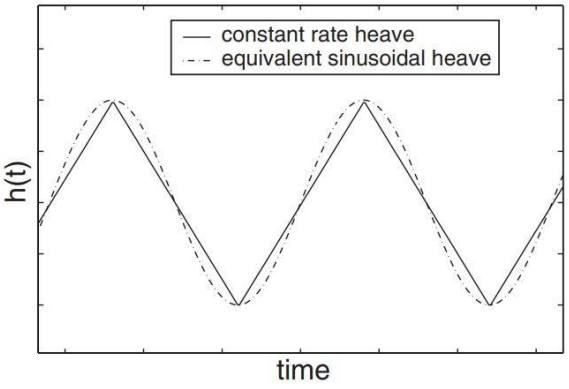

Figure 2.11: Qualitative plot showing constant rate heaving motion and its equivalent sinusoidal heaving motion [42].

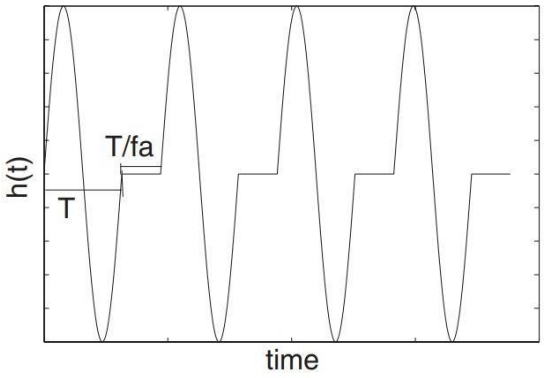

Figure 2.12: Schematic plot of a heaving motion described by a sinusoid followed by a gap, heave is zero during *T/fa*, *fa* is a fraction of the sinusoidal time period [42].

A tandem airfoil arrangement was first proposed by Schmidt [43] in 1965 to improve the propulsive efficiency of the single flapping airfoil mechanism. By placing a stationary airfoil on the wake of the flapping airfoil, the propulsive efficiency doubles by converting the vortical energy generated by the airfoil in front into additional thrust. Later, Tuncer and Platzer [44] through a numerical method using a Reynolds Averaged Navier-Stokes (RANS) solver, determined the thrust and propulsive efficiency of a NACA0012 airfoil in single flapping and flapping/stationary configurations. The obtained results showed an improvement in total propulsive efficiency from 50% with the single flapping configuration, for a reduced frequency of 0.75 and an amplitude per chord length of 0.20, to 70% with the flapping/stationary

configuration, for a stationary airfoil positioned at two chord lengths horizontally and one chord length vertically of the flapping airfoil. The flapping/stationary configuration is displayed in Figure 2.13.

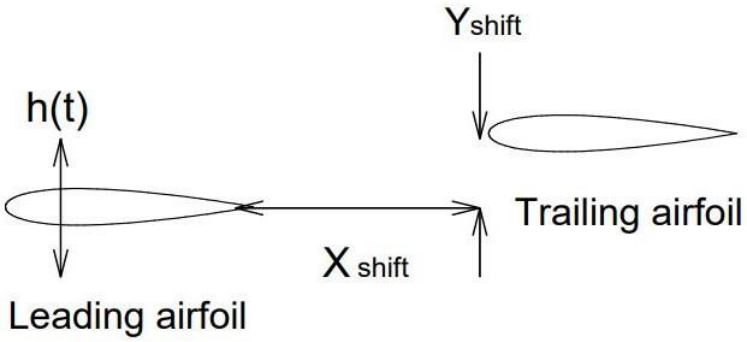

Figure 2.13: Airfoils in tandem configuration [44].

More recently, Kinsey and Dumas [45] conducted a numerical research based on 2D URANS simulations. The purpose of the investigation was to find an optimal spatial setup for two flapping foils within a hydrokinetic turbine, to maximize the energy extraction efficiency of the turbine. The authors concluded that the downstream foil placement plays a crucial role in the accomplishment of that purpose. If placed correctly, the downstream foil profits from added dynamic pressure by the induced velocities from the upstream foil wake vortices. Yet, if placed incorrectly, the interaction of the downstream foil with the wake may reduce the total efficiency to values lower than the single flapping foil configuration.

Kinsey and Dumas [45] used a parameter that characterizes the position of both foils, by blending the spacing and motion phase-shift, to predict different favorable spatial arrangements. However, this parameter can only be used for cases with the same motion amplitude and frequency. It should be noted that this numerical analysis may overpredict the power extraction efficiency since the gain due to the interaction of the downstream foil with the wake vortices may have more impact in the 2D case, when compared to the three-dimensional case.

Orienting the flapping wing mechanism to its possible application in the aeronautical industry as a substitute for the traditional individual thrust and lift mechanisms, Ashraf et al. [46] studied the potential advantages of using the flapping-wing mechanisms on a High-Altitude Long-Endurance (HALE) aircraft. The results showed that, for a pure plunging motion, the efficiency obtained would be too little to be considered a viable solution. However, for flapping motion, which combines both pitching and plunging motions, the resulting efficiency proved to be satisfactory for this mechanism to substitute the conventional propulsive mechanism.

Numerous researches focused on the understanding of the flapping wing mechanism, and the aerodynamic phenomenons that it involves, were made, however, this problem requires

more investigation in order to be able to implement and use this mechanism in a profitable way. This includes investigating in what ways it may reduce or even not rely on the use of fossil fuels and move towards sustainable energy sources. To fully understand the physics and how to optimize the overall aerodynamic performances of this wing configuration, exhaustive numerical and experimental studies relative to the physical properties of the airfoil, foils configuration, governing parameters, and operating regimes are still required.

Chapter 3

Methodology

This chapter exposes the mathematical tools and methodology used for the simulations of the problem, followed by the numerical methodology, and concluding with its numerical validation to ensure the reliability of the solution.

3.1 Mathematical Models

The mathematical models used in this dissertation include the governing equations used to predict the effects of the turbulent flow, the turbulence model used to solve these equations, and lastly, the wall boundary conditions selected accordingly to the mesh used for this problem.

3.1.1 Governing Equations

Several approaches were used throughout the investigation of the flapping wing mechanism. Being them experimental or numerical, and despite the methods progressive improvement, the understanding of the aerodynamic phenomena behind this problem is still complex and needs further investigation. In this study, a numerical approach is adopted, using a Reynolds Averaged Navier-Stokes (RANS) formulation to predict the effects of the turbulent flow. Later the methodology was validated by comparison with the results obtained experimentally by Marques [4].

As stated in [47], the RANS equations govern the transport of the averaged flow quantities, with the whole range of the scales of turbulence being modeled, which results in a great reduction of the computational resources needed to obtain the results.

The continuity and momentum averaged equations are solved in order to obtain the mean velocity field. These equations are, respectively, defined as

$$\frac{\partial \rho}{\partial t} + \frac{\partial}{\partial x_i}(\rho u_i) = 0 \tag{3.1}$$

$$\frac{\partial}{\partial t}(\rho u_i) + \frac{\partial}{\partial x_j}(\rho u_i u_j) = -\frac{\partial p}{\partial x_i} + \frac{\partial}{\partial x_j}\left[\mu\left(\frac{\partial u_i}{\partial x_j} + \frac{\partial u_j}{\partial x_i} - \frac{2}{3}\delta_{ij}\frac{\partial u_l}{\partial x_l}\right)\right] + \frac{\partial}{\partial x_j}(-\rho\overline{u_i' u_j'}) \tag{3.2}$$

However, despite having the same general form as the instantaneous Navier-Stokes equations, when these equations get converted to the RANS equations, new terms that represent

the effects of turbulence appear. These terms are Reynolds stresses, $-\rho\overline{u_i' u_j'}$, and must be modeled to solve the equations. The Boussinesq hypothesis relates the Reynolds stresses to the mean velocity gradients via an eddy viscosity approach, which means that the Reynolds stress terms are expressed in terms of mean flow quantities. This hypothesis is defined as

$$-\rho\overline{u_i' u_j'} = \mu_t \left(\frac{\partial u_j}{\partial x_j} + \frac{\partial u_j}{\partial x_i} \right) - \frac{2}{3} \left(\rho k + \mu_t \frac{\partial u_k}{\partial x_k} \right) \delta_{ij} \tag{3.3}$$

where μ_t is the turbulent viscosity and k is the turbulence kinetic energy and its defined by

$$k = \frac{1}{2} \overline{u_i' u_i'} \tag{3.4}$$

To solve the RANS equations, an eddy viscosity model is selected to be used to calculate the turbulent viscosity term, which in turn allows calculating the Reynolds stress term. This model is included in a class of turbulence models based on the eddy viscosity approach.

3.1.2 Turbulence Modeling

For this work, it was necessary to select a turbulent model capable of presenting good behavior at predicting boundary layers with adverse pressure gradients while maintaining the ability to capture the characteristics of the mean flow. Thus, the Shear-Stress Transport (SST) k – ω model [48] was chosen.

This turbulence model surpasses the flaws presented by the k – ε and k – ω models alone by blending them in such a way that allows conciliating the free-stream independency of the first with the robust and accurate formulation of the second in the near-wall region.

In the SST k – ω model used in this work [47], the transport equations for k and ω are, respectively, expressed as follows:

$$\frac{\partial}{\partial t}(\rho k) + \frac{\partial}{\partial x_i}(\rho k u_i) = \frac{\partial}{\partial x_j} \left(\Gamma_k \frac{\partial k}{\partial x_j} \right) + \tilde{G}_k - Y_k + S_k \tag{3.5}$$

$$\frac{\partial}{\partial t}(\rho \omega) + \frac{\partial}{\partial x_i}(\rho \omega u_i) = \frac{\partial}{\partial x_j} \left(\Gamma_\omega \frac{\partial \omega}{\partial x_j} \right) + G_\omega - Y_\omega + D_\omega + S_\omega \tag{3.6}$$

where Γ_k and Γ_ω represent the effective diffusity of turbulence kinetic energy, k, and specific dissipation rate, ω, respectively; $\tilde{G}_k$ and G_ω represent the generation of k due to mean velocity gradients, and ω; Y_k and Y_ω are the dissipation of k and ω due to turbulence; D_ω is the cross-diffusion term; and S_k and S_ω are the user-defined source terms.

The effective diffusity terms are defined as

$$\Gamma_k = \mu + \frac{\mu_t}{\sigma_k} \tag{3.7}$$

$$\Gamma_\omega = \mu + \frac{\mu_t}{\sigma_\omega} \tag{3.8}$$

with μ_t being the turbulent viscosity with σ_k and σ_ω being, respectively, the turbulent Prandtl numbers for k and ω. These terms are defined as

$$\mu_t = \frac{\rho k}{\omega} \frac{1}{\max\left[\frac{1}{a^*}, \frac{SF_2}{a_1\omega}\right]} \tag{3.9}$$

$$\sigma_k = \frac{1}{F_1/\sigma_{k,1} + (1 - F_1)/\sigma_{k,2}} \tag{3.10}$$

$$\sigma_\omega = \frac{1}{F_1/\sigma_{\omega,1} + (1 - F_1)/\sigma_{\omega,2}} \tag{3.11}$$

where S is the strain magnitude and a^* is given by

$$a^* = a^*_\infty \left(\frac{a_0^* + Re_t/R_k}{1 + Re_t/R_k}\right) \tag{3.12}$$

with

$$Re_t = \frac{\rho k}{\mu\omega} \tag{3.13}$$

$$R_k = 6 \tag{3.14}$$

$$a^*_0 = \frac{\beta_i}{3} \tag{3.15}$$

$$\beta_i = 0.072 \tag{3.16}$$

The blending functions used by SST k – ω turbulence model are defined by the following equations:

$$F_1 = \tanh(\Phi_1^4) \tag{3.17}$$

$$\Phi_1 = \min\left[\max\left(\frac{\sqrt{k}}{0.09\omega y}, \frac{500\mu}{\rho y^2 \omega}\right), \frac{4\rho k}{\sigma_{\omega,2} D^+_\omega y^2}\right] \tag{3.18}$$

$$D^+_\omega = \max\left[2\rho \frac{1}{\sigma_{\omega,2}} \frac{1}{\omega} \frac{\partial k}{\partial x_j} \frac{\partial \omega}{\partial x_j}, 10^{-10}\right] \tag{3.19}$$

$$F_2 = \tanh(\Phi_2^2) \tag{3.20}$$

$$\Phi_2 = \max\left(2\frac{\sqrt{k}}{0.09\omega y}, \frac{500\mu}{\rho y^2 \omega}\right) \tag{3.21}$$

where y is the distance to the closest surface and D_ω^+ is the positive portion of the cross-diffusion term.

In terms of modeling the turbulence production, the production of k and ω are, respectively, given by the terms $\tilde{G}_k$ and G_ω, being defined as

$$\tilde{G}_k = \min(G_k, 10\rho\beta^* k\omega) \tag{3.22}$$

$$G_\omega = \alpha\frac{\omega}{k}\tilde{G}_k \tag{3.23}$$

where G_k is modeled as

$$G_k = -\rho\overline{u_i' u_j'}\frac{\partial u_j}{\partial x_i} = \mu_t S^2 \tag{3.24}$$

The coefficient α relative to Equation (3.23) is given by

$$\alpha = \frac{\alpha_\infty}{\alpha^*}\frac{\alpha_0 + Re_t/R_\omega}{1 + Re_t/R_\omega} \tag{3.25}$$

with $R_\omega = 2.95$ and where α_∞ is defined as follows:

$$\alpha_\infty = F_1\alpha_{\infty,1} + (1 - F_1)\alpha_{\infty,2} \tag{3.26}$$

$$\alpha_{\infty,1} = \frac{\beta_{i,1}}{\beta_\infty^*} - \frac{\kappa^2}{\sigma_{w,1}\sqrt{\beta_\infty^*}} \tag{3.27}$$

$$\alpha_{\infty,2} = \frac{\beta_{i,2}}{\beta^*_\infty} - \frac{\kappa^2}{\sigma_{w,2}\sqrt{\beta_\infty^*}} \tag{3.28}$$

with $\kappa = 0.41$.

The turbulence dissipation of the transport equations are represented by the terms Y_k and Y_ω of the Equations (3.5) and (3.6).

The term representing the dissipation of turbulence kinetic energy is defined as

$$Y_k = \rho\beta^* k\omega \tag{3.29}$$

with

$$\beta^* = \beta_i^* \left[1 + \zeta^* F(M_t)\right] \tag{3.30}$$

$$\beta_i^* = \beta_\infty^* \frac{4/15 + (Re_t/R_\beta)^4}{1 + (Re_t/R_\beta)^4} \tag{3.31}$$

$$\zeta^* = 1.5 \tag{3.32}$$

$$R_\beta = 8 \tag{3.33}$$

$$\beta_\infty^* = 0.09 \tag{3.34}$$

The term representing the dissipation of ω is defined as

$$Y_\omega = \rho\beta\omega^2 \tag{3.35}$$

with

$$\beta = \beta_i \left[1 - \frac{\beta_i^*}{\beta_i}\zeta^* F(M_t)\right] \tag{3.36}$$

$$\beta_i = F_1\beta_{i,1} + (1 - F_1)\beta_{i,2} \tag{3.37}$$

As previously referred, this turbulence model came from the adaptation of the standard $k-\varepsilon$ and standard $k-\omega$ models. The blend of these two turbulence models originated a cross-diffusion term in the transport equation for ω, Equation (3.6), and it is defined as

$$D_\omega = 2(1 - F_1)\rho\sigma_{\omega,2}\frac{\partial k}{\partial x_j}\frac{\partial \omega}{\partial x_j} \tag{3.38}$$

An overview of the $k-\omega$ turbulence model constants is presented in the table below.

a_1	0.31	β_∞^*	0.09
a_∞^*	1	$\beta_{i,1}$	0.075
a_∞	0.52	$\beta_{i,2}$	0.0828
a_0	1/9	$\sigma_{k,1}$	1.176
R_k	6	$\sigma_{\omega,1}$	2.0
R_ω	2.95	$\sigma_{k,2}$	1.0
R_β	8	$\sigma_{\omega,2}$	1.168
M_{t0}	0.25	ζ^*	1.5

Table 3.1: SST $k-\omega$ turbulence model constants.

The SST $k-\omega$ turbulence model uses a near-wall model approach, which means the near-wall region is solved all the way down to the wall, as shown in Figure 3.1.

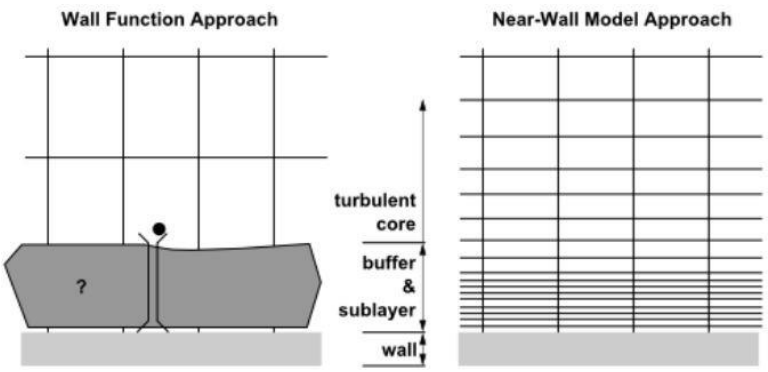

Figure 3.1: Near-wall treatment approaches [47].

Thus, it is essential to ensure a good representation of the effects of the flow near the walls. The dimensionless distance from the cell centroid to the nearest wall is represented as y^+, being an important parameter in turbulence modeling to guarantee accurate computed results.

This dimensionless distance is scaled on the flow conditions, meaning that if the free-stream flow conditions or the shape and size of the geometry change, the boundary layer profile still develops and scales correctly. The y^+ is defined as

$$y^+ = \frac{\rho u_\tau y_p}{\mu} \tag{3.39}$$

where ρ is the fluid density, y_p is the distance from the cell centroid to the nearest wall, μ is the kinematic viscosity, and u_τ is the friction velocity.

The u_τ is based on the wall shear stress, τ_w, as represented in Equation (3.40).

$$u_\tau = \sqrt{\tau_w/\rho} \tag{3.40}$$

The y^+ value is obtained via a method where the y^+ is a function of the wall shear stress, τ_w, as shown in Equation (3.41), and, in turn, the τ_w depends on y^+, as shown in Equation (3.42).

$$y^+ = \frac{\rho y_p \sqrt{\tau_w/\rho}}{\mu} \tag{3.41}$$

$$\tau_w/\rho = \nu \left(\frac{y^+}{\frac{1}{\kappa}\log(Ey^+)} \right)^{!} \frac{U_p}{y_p} \tag{3.42}$$

To ensure that the wall shear stress is calculated correctly for this turbulence model, the dimensionless distance normal to the wall is kept on the Viscous Sub-layer of the near-wall

region, $y^+ < 5$, represented in Figure 3.2. In this region, viscosity plays a major role in momentum and mass transfer, opposite to the Log-law Region where the turbulence influence is dominant. However, the y^+ value is kept at $y^+ \approx 1$ to improve the accuracy of the results because the shape of the universal profile used near the transition to the buffer region can vary when in presence of strong curvatures, adverse pressure gradients, or separation.

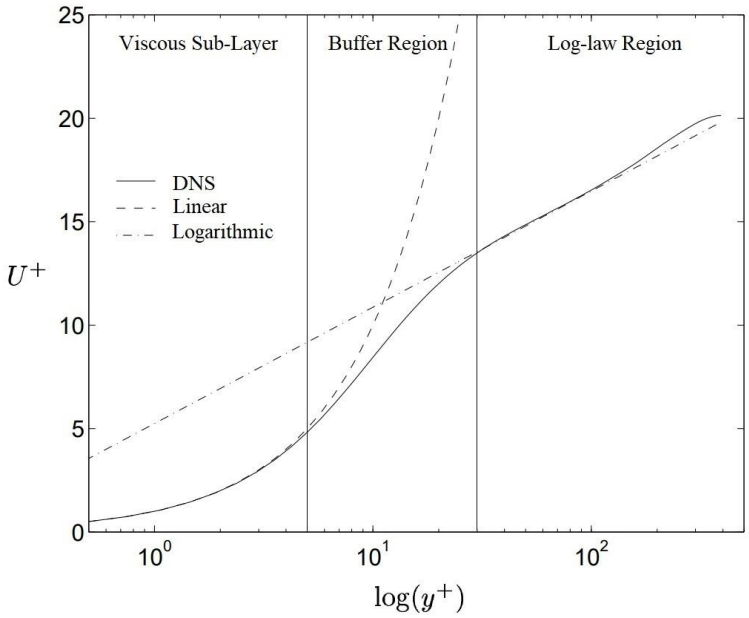

Figure 3.2: Subdivisions of the near-wall region (adapted from [49]).

3.1.3 Wall Boundary Conditions

The wall boundary conditions for the k equation in the SST k–ω turbulence model are treated differently accordingly to the mesh used. For wall-function meshes, the boundary conditions will follow a wall function approach. However, for the fine meshes, the appropriate low-Reynolds number boundary conditions will be applied.

For the ω equation, its value at the wall is specified by Equation (3.43).

$$\omega_w = \frac{\rho\,(u^*)^2}{\mu}\omega^+ \tag{3.43}$$

where ω^+ can be given by Equations (3.44) or (3.45) for the viscous sublayer and the logarithmic region, respectively.

$$\omega^+ = \frac{6}{\beta_i\,(y^+)^2} \tag{3.44}$$

$$\omega^+ = \frac{1}{\sqrt{\beta^*_\infty}}\frac{du^+}{dy^+} \tag{3.45}$$

In this study, a fine mesh is used since the dimensionless distance normal to the wall is kept on the viscous sublayer, $y^+ \approx 1$, to guarantee the accuracy of the turbulence model used. A wall treatment, which switches automatically from the viscous sublayer formulation to the wall function, is defined for the ω-equation, resulting in a grid-independent solution of the skin friction value.

3.2 Numerical Methodology

Next, the problem formulation, which exhibits the configuration of the flat plates and the implementation of their motion, is exposed. It is followed by the mesh configuration, the placement of the domain boundaries, finishing with the presentation of the numerical setup of the simulation.

3.2.1 Problem Formulation

Flat plates undergoing a sinusoidal plunging motion are analyzed to understand the impact of different trailing edges on the resultant vortical structures of the wake and the propulsive efficiency. Furthermore, the dependency between those structures and the governing parameters of the problem is studied.

Two different flat plates are used in this study. Both present a 100 mm chord, a 5 mm thickness, and a leading-edge symmetrically sharpened, having the edge a 6 mm length (corresponding to approximately 22.62° relatively to the centerline of the thickness). The difference between the flat plates is relative to the trailing edge, being one of them straight, and the other one presenting the same shape as the leading edge. The flat-plates' geometry is displayed in Figure 3.3.

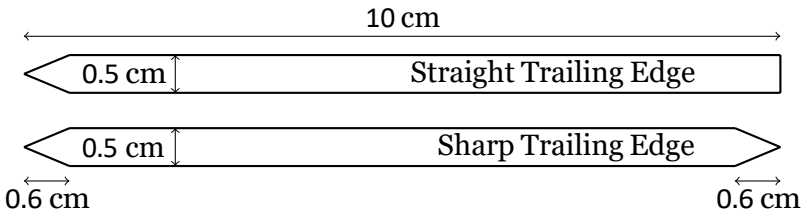

Figure 3.3: Flat plates considered.

The position and velocity of the flat plates during this movement are given by Equations (3.46) and (3.47), respectively, which are defined as

$$y(t) = A\sin(2\pi ft) \tag{3.46}$$

$$\dot{y}(t) = 2\pi f A\cos(2\pi ft) \tag{3.47}$$

where A is the plunging amplitude and f is the plunging frequency.

However, to implement the flat-plates' motion on the ANSYS software a different approach was required because, as the foil starts its movement at the central position, its initial velocity would be the maximum velocity, possibly leading to computational errors and difficulty in converging a periodic solution.

The motion implementation was executed resorting to a User-Defined Function (UDF), where the flat-plate's velocity profile was divided into two sections, being defined by Equation (3.48) as

$$\dot{y}(t) = \begin{cases} \frac{\pi f A}{2} \cos\left(\pi f t - \frac{\pi}{2}\right) & \text{if } t \leq T \\ 2\pi f A \cos\left[2\pi f\left(t + \frac{1}{4}T\right)\right] & \text{if } t > T \end{cases} \tag{3.48}$$

where $T = 1/f$ and represents the period of the motion.

Initially, the plate follows a sinusoidal upwards movement with half of the amplitude and frequency of the desired motion. In this section, the foil starts the motion with zero velocity, finishing at the highest point of the trajectory after one period. Afterward, the foil enters the second section of the movement where it follows the desired motion, starting from the highest point. This model of the velocity profile helps stabilize and converge a periodic solution. For better visualization, the position of the flat plate throughout time is displayed in Figure 3.4.

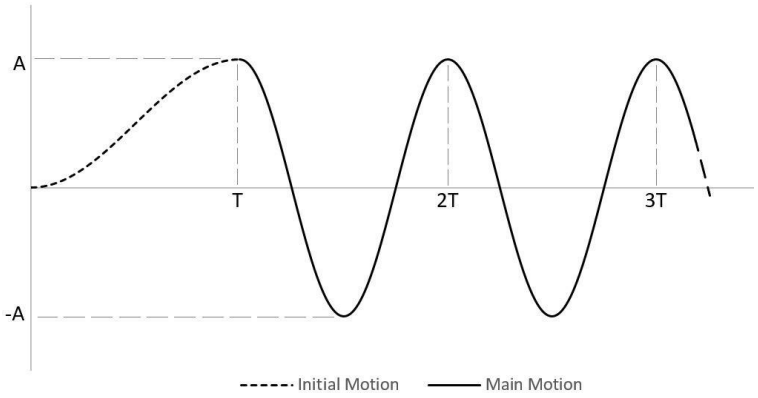

Figure 3.4: Flat-plate's trajectory.

3.2.2 Mesh Configuration

The formulation of this problem implies unsteady characteristics and moving airfoils. Thus, the simulations were executed using a dynamic mesh with an overset configuration instead of adopting a deforming mesh, which allows guaranteeing the orthogonality of the mesh and thus does not degrade its quality during simulations.

The mesh structure is divided into two separated meshes: one mesh around the component, and one mesh for the background, as represented in Figure 3.5. The first surrounds the airfoil, following its motion, and the cells' size increases in a direction normal to the flat-plates' surface. On the other hand, the background mesh is static and presents two main zones, being the cells' size constant in a square region around the foil's central position, with

a dimension of two times the chord of the foil, and progressively increasing in the direction of the boundaries of the domain.

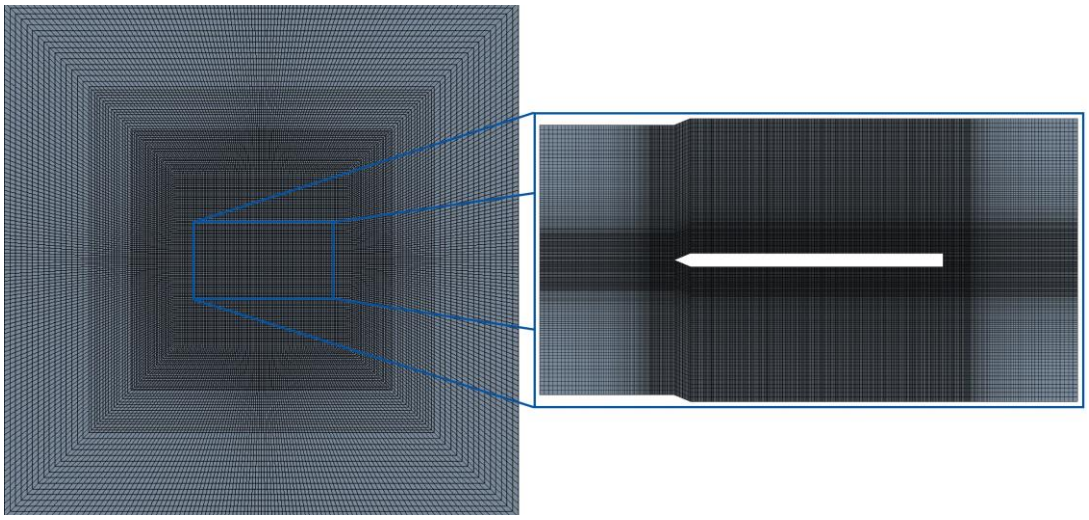

Figure 3.5: Background (left) and flat-plate's (right) meshes.

3.2.3 Boundary Location

The study executed to avoid the influence of the blockage effect in the solution followed the same method used by Camacho [14]. Contrarily to the typical blockage ratio given by a relation between the thickness and length of the airfoil, the upper and lower walls' distance to the airfoil was evaluated taking into account the airfoil's motion. In this method, the blockage ratio is given by

$$\zeta = \frac{2A + t}{L} \tag{3.49}$$

where A is the plunging amplitude, t is the thickness of the foil, and L is the inlet length.

According to Camacho's study, a 10% blockage ratio was considered to be an acceptable value to avoid the influence of the walls' location on the obtained results, being this value used for the calculation of the inlet height. Regarding the remaining parameters, the maximum plunging amplitude considered in this study was used, having a value of 28 mm, and the flat plates in use presented a thickness of 5 mm.

This study resulted in an inlet length value of 610 mm, being the upper and lower walls positioned at 305 mm each from the central position of the flat plate. The inlet and outlet were placed at the same distance from the center of the domain as the walls, being this distance considered to have no influence on the flow field around the plunging foil.

The boundaries location selected allowed a square-shaped flow field domain, resulting in a simpler mesh geometry. Furthermore, the implementation of this method allowed not only to guarantee the quality of the obtained results but also to avoid the over-dimensioning of

the domain that would result in additional computational cost.

3.2.4 Numerical Setup

Having implemented the boundary location method, the boundary conditions were defined. Four boundaries are considered in this problem: the inlet, the outlet, the upper and lower walls, and the airfoil. The inlet is a velocity inlet specified by the velocity magnitude normal to the boundary, located on the left side of the background mesh. The outlet adopted is a pressure outlet where the pressure value is equal to the inlet's pressure, remaining constant throughout the domain, and it's placed on the right side of the background mesh. The upper and lower walls, corresponding to the upper and lower boundaries of the flow field domain, respectively, are admitted to have no shear stress, eliminating the boundary layer effects on them. At last, the airfoil is considered as a wall with the no-slip condition.

The numerical solution methods selected to compute the results must be chosen accordingly to the formulation and conditions of the problem to minimize possible errors and guarantee the accuracy of the solution. As aforementioned, a dynamic mesh with an overset configuration was used for this problem, limiting the available methods to obtain a periodic solution.

Regarding the spatial discretization, the evaluation of the gradients was executed according to the Least Squares Cell-Based method. These gradients are needed to discretize the convection and diffusion terms in the flow conservation equations.

To discretize the momentum equation, the pressure field and face mass fluxes are needed and must be obtained as a part of the solution. Hence, the pressure interpolation scheme chosen was PRESTO! (PREssure STaggering Option).

The Second-Order Upwind Scheme was selected to discretize the momentum, turbulent kinetic energy, and specific dissipation rate. This scheme computes the values at the cell faces through a multidimensional linear reconstruction approach, allowing a higher-order accuracy. The face values, ϕ_f, are obtained as shown in Equation (3.50)

$$\phi_f = \phi + \nabla\phi \cdot \vec{r} \tag{3.50}$$

where ϕ is the cell-centered value, $\nabla\phi$ is its gradient in the upstream cell, and $\vec{r}$ is the displacement vector from the upstream cell centroid to the face centroids. Additionally, to avoid adding false new maxima or minima cell values, the gradients are limited.

The Pressure-Velocity Coupling was achieved using the coupled algorithm that solves the momentum equation and the pressure-based continuity at the same time. This is obtained through implicit discretization of the pressure gradient terms in the momentum equations, and the face mass flux.

Lastly, for the transient formulation, the temporal discretization for the time-dependent

equations was solved using the First-Order-Implicit method, which was the only available method when using an overset mesh.

For the solution, a hybrid initialization was used, which is composed of a compilation of recipes and boundary interpolation methods. This initialization solves the Laplace equation to produce a velocity field that conforms to complex domain geometries, and a pressure field that smoothly connects high and low-pressure values in the computational domain.

3.3 Numerical Validation

The validation of the numerical model comprises the independence studies of the mesh and the time step. Furthermore, a comparison with experimental data is done to guarantee the valid prediction of the main characteristics of the mean flow.

3.3.1 Mesh Independence Study

To guarantee the viability of the obtained results, it was necessary to ensure that the meshes in use did not influence the solution. Thus, the simulation was executed with three meshes with different levels of refinement, being the meshes refined by roughly doubling the cells of the previous one.

The parameters used to compare the solutions and validate the mesh independence study were the lift and drag coefficients.

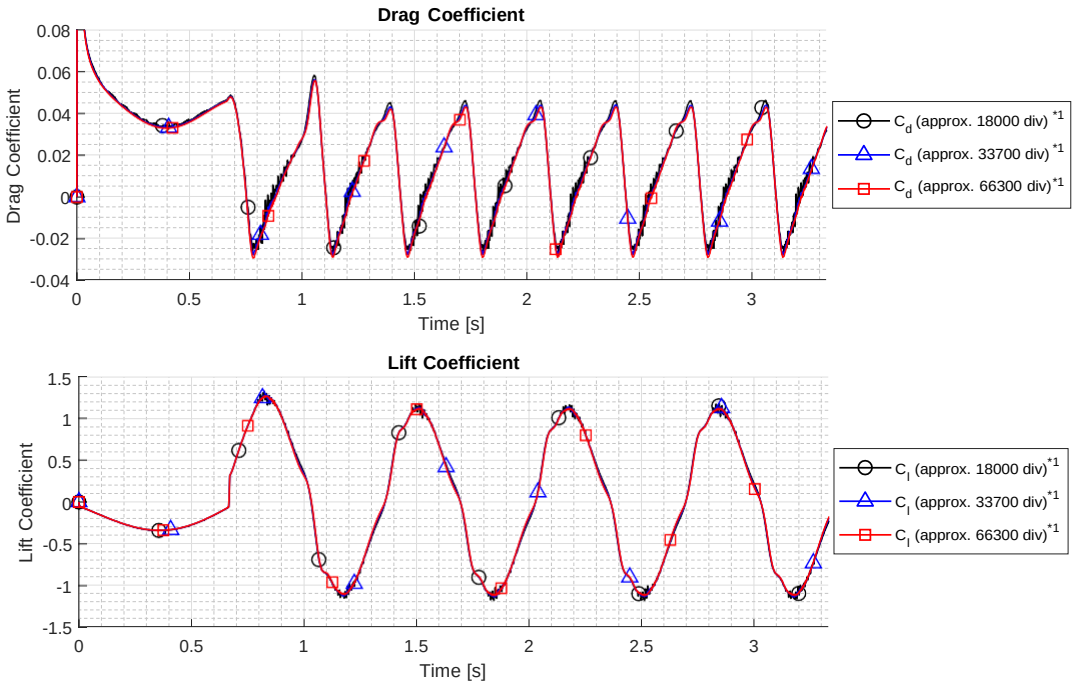

Figure 3.6: Parameters evolution for different meshes with $U_\infty = 1.0\ m/s$, $A = 28\ mm$, and $f = 1.5\ Hz$. (*1 Divisions of the background mesh)

As displayed in Figure 3.6, the similarity between the results obtained with the different meshes for both parameters shows that the solution is not dependent on the selected mesh. With the mesh independence concluded, the component and background meshes with medium refinement level were selected to proceed to the time-step independence study.

3.3.2 Time-Step Independence Study

Due to the periodic characteristics of simulation, a time-step independence study was necessary to guarantee that the time step used did not influence the results.

Similarly to the mesh independence study, the lift and drag coefficients were the parameters used to verify the independence of the results with three different time steps, being the time steps per period doubled for each simulation (T/200 s, T/400 s, and T/800 s). It is relevant to point out that, for this study, the characteristics of the flat-plate's movement were kept the same as the one used for the mesh independence study.

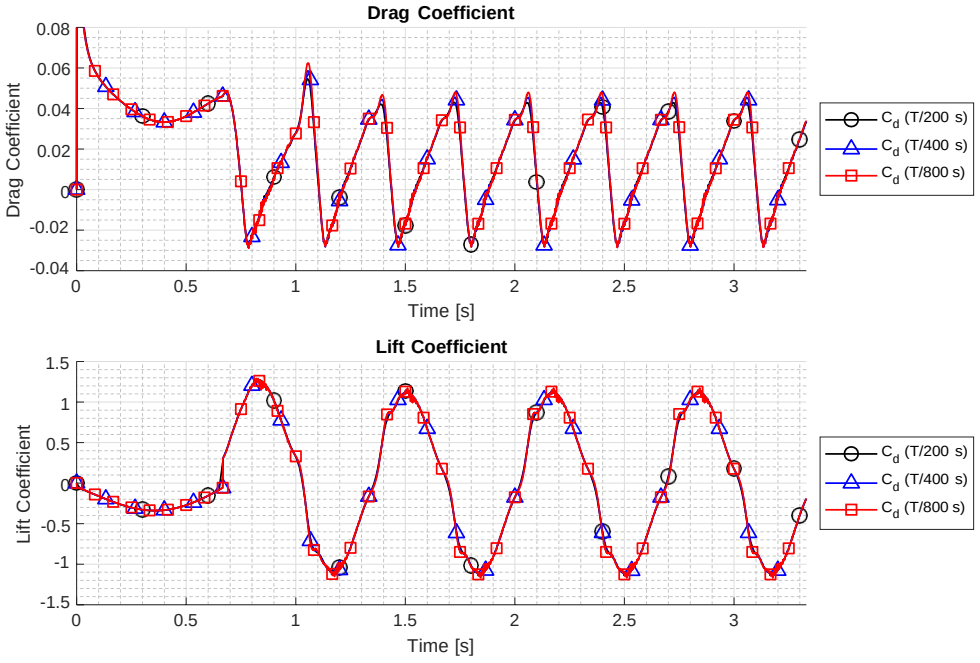

Figure 3.7: Parameters evolution for different time steps with $U_\infty = 1.0\ m/s$, $A = 28\ mm$, and $f = 1.5\ Hz$.

As shown in Figure 3.7, the variation of time step presents almost no influence on the results obtained, concluding the time-step independence study and the numerical validation. For the problem simulation, the time step selected was T/400 s.

3.3.3 Numerical and Experimental Comparison

A comparison between the simulation and experimental data is required to approve the numerical method used and guarantee the viability of the obtained periodic solution. The problem formulation investigated by Marques [4] presents similarities in the flat-plate's charac-

teristics and movement and the flow field properties. Thus, three cases were used to qualitatively validate the numerical methodology with the experimental data obtained by Marques.

To guarantee the agreement between the simulation and the experiment, the experimental and numerical trajectories of the flat plate were analyzed. The similarity displayed in Figure 3.8 between the flat-plate's movement in both studies allows comparing the results to approve the numerical simulation.

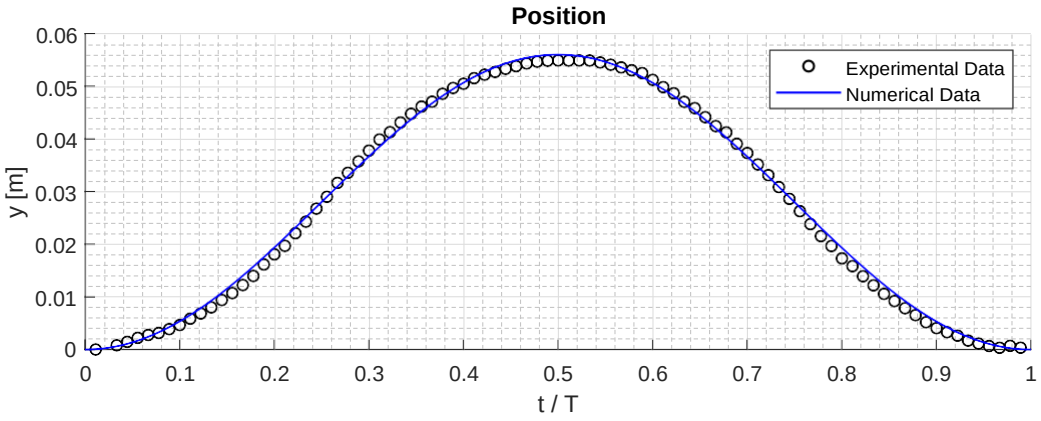

Figure 3.8: Comparison between the experimental and numerical trajectories of the flat plate.

Therefore, three simulations were compared with Marques' experimental data to validate the numerical setup. The geometric and kinematic parameters were kept identical for the different cases, with a reduced frequency of 1.89 and a nondimensional amplitude of 0.28. The free-stream speed was the only parameter varying between the cases, assuming the values of 0.25 m/s, 0.5 m/s, and 1 m/s, which correspond to Reynolds numbers of 7.8×10^2, 1.6×10^3, and 3.1×10^3.

The total pressure contour obtained using CFD was used to compare the numerical results with the flowfield observed experimentally, for each of the three cases. In Figures 3.9, 3.10, and 3.11, four different stages of the period were analyzed ($t/T = 0.25, 0.50, 0.75, 1.00$).

The numerical results display an accurate prediction of the main features of the mean flow. In the simulations, the LEVs formation and evolution, its convection, and separation were properly predicted, being the similarities more apparent at lower Reynolds number, where the vertical motion of the flat plate has more influence on the vortical formations in the mean flow. This comparison allows verifying the numerical methodology used for the simulations, enabling their use for the rest of the study.

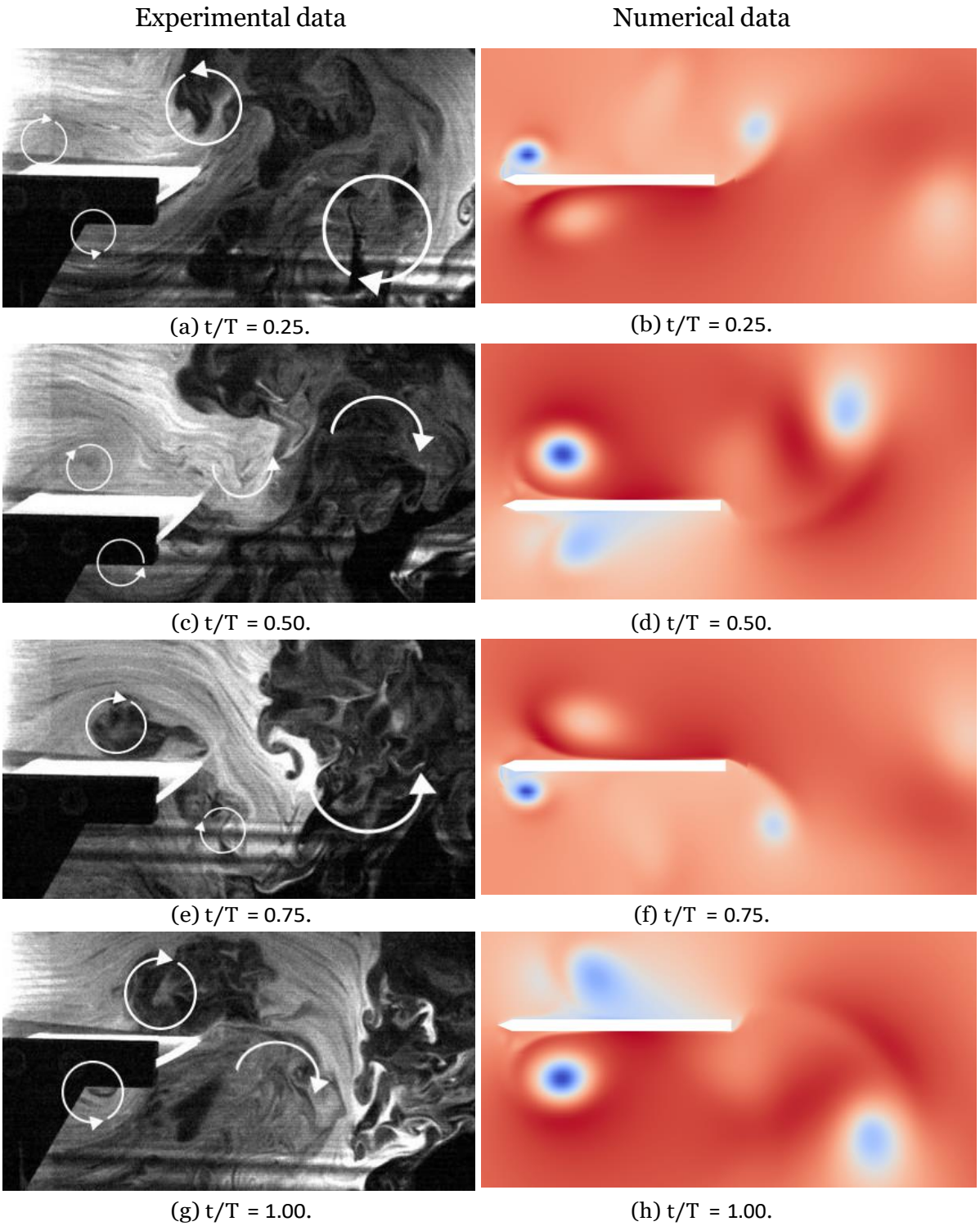

Figure 3.9: Comparison between the experimental and numerical results for $Re = 7.8 \times 10^2$.

Experimental data | Numerical data

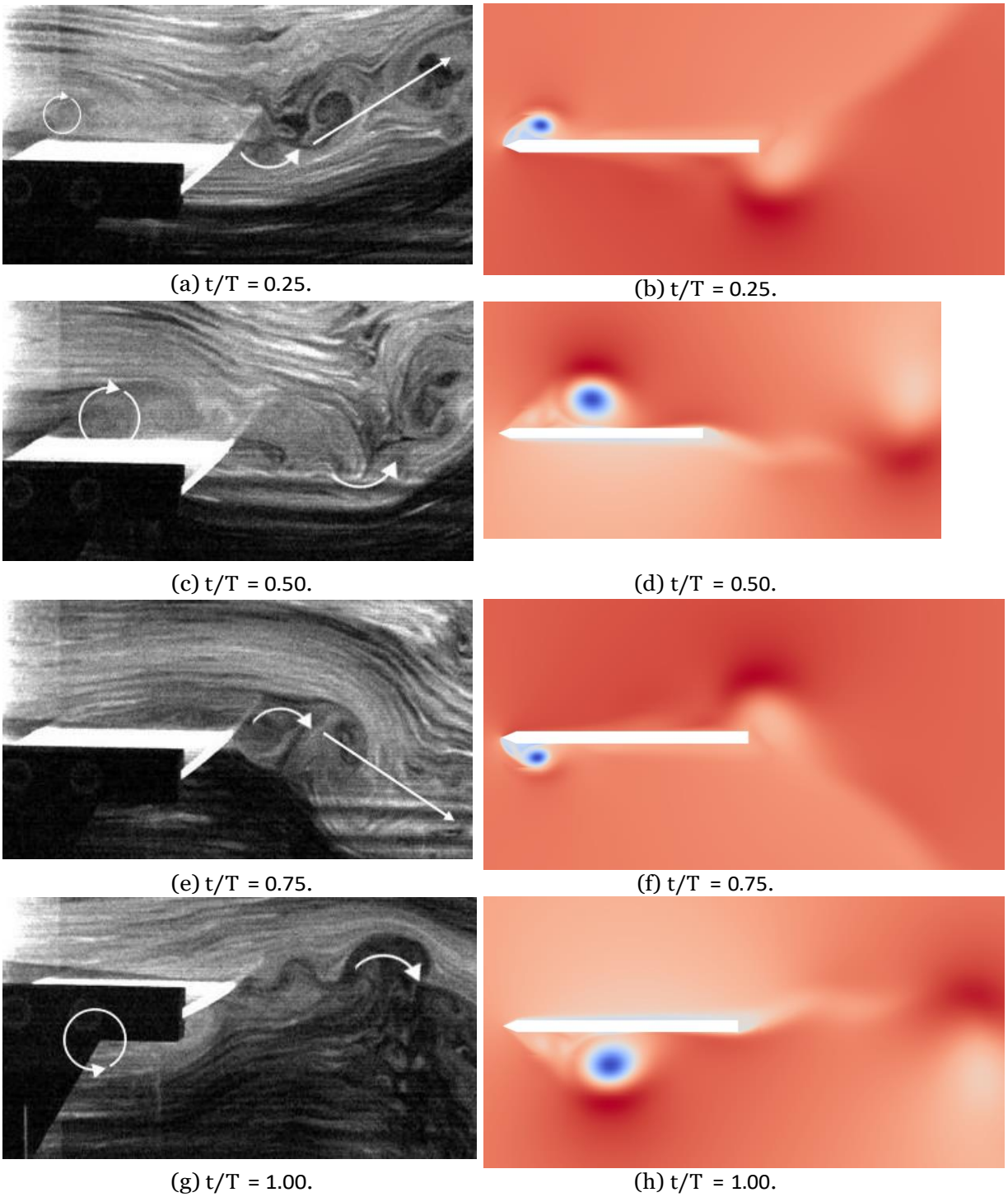

(a) t/T = 0.25. (b) t/T = 0.25.

(c) t/T = 0.50. (d) t/T = 0.50.

(e) t/T = 0.75. (f) t/T = 0.75.

(g) t/T = 1.00. (h) t/T = 1.00.

Figure 3.10: Comparison between the experimental and numerical results for $Re = 1.6 \times 10^3$.

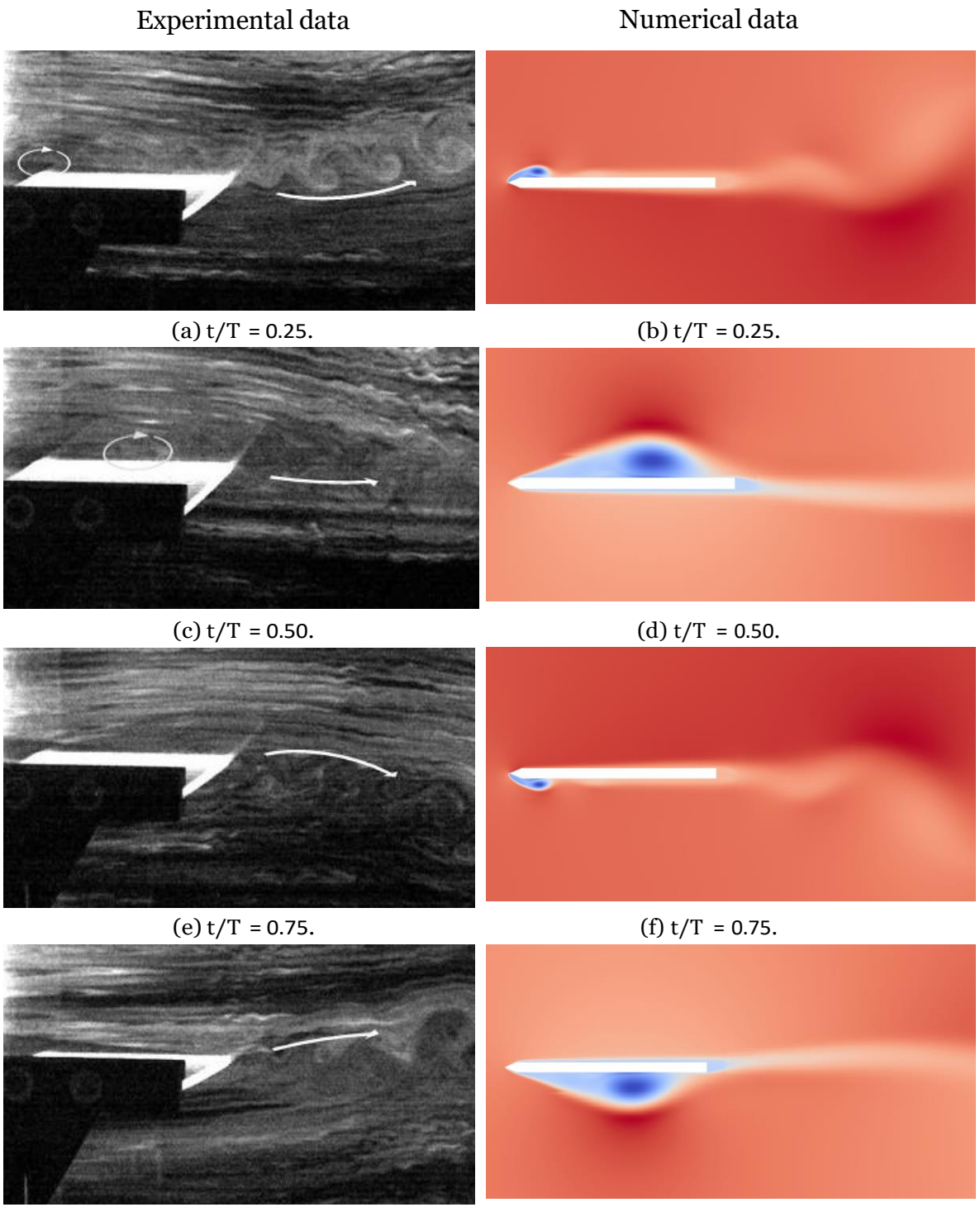

Figure 3.11: Comparison between the experimental and numerical results for $Re = 3.1 \times 10^3$.

Chapter 4

Results and Discussion

This chapter shows the influence of different trailing edge shapes of flat plates undergoing pure plunging motion on the aerodynamic forces produced. Furthermore, the impact of the variation of kinematic parameters such as the reduced frequency, k, and nondimensional amplitude, h, on these forces is analyzed. This chapter is complemented with a discussion on the matter.

In this study, two flat plates with different trailing-edge shapes undergoing pure plunging motions were analyzed to understand their influence on the aerodynamic forces produced. The flat-plates' motions are given by a reduced frequency and a nondimensional amplitude ranging between $1 \leq k \leq 5$ and $0.125 \leq h \leq 0.500$, respectively. The thrust and power coefficients were the selected parameters to observe such influence, followed by the effort to relate these coefficients' behavior with the flow field features. These two coefficients are given by

$$C_t = -C_d \tag{4.1}$$

and

$$C_P = -C_l \frac{\dot{y}}{U_\infty} \tag{4.2}$$

respectively. The mean values of these coefficients were calculated based on the last period simulated, guaranteeing the closest result to a periodic solution.

The numerical cases simulated for both studied flat plates are exhibited in Table 4.1, being shown the kinetic parameters h, k, and kh, followed by the mean values of thrust and power coefficients.

The domain of reduced frequency was divided with a maximum k step of 0.5 between each case. Although, for h values of 0.250 and 0.500, some additional cases were simulated to properly capture the behavior of the performance parameters. For $h = 0.500$, the maximum k value simulated is limited by the non-convergence of the solution due to the high-velocity motions of these conditions.

h	k	kh	St	Straight TE		Sharp TE	
				$\overline{C_P}$	$\overline{C_t}$	$\overline{C_P}$	$\overline{C_t}$
0.125	1.00	0.1250	0.0398	0.0291	-0.0324	0.0268	-0.0321
	1.50	0.1875	0.0597	0.0600	-0.0232	0.0537	-0.0228
	2.00	0.2500	0.0796	0.1076	-0.0176	0.0932	-0.0169
	2.50	0.3125	0.0995	0.1779	-0.0141	0.1500	-0.0132
	3.00	0.3750	0.1194	0.2684	-0.0083	0.2242	-0.0112
	3.50	0.4375	0.1393	0.3873	-0.0023	0.3156	-0.0016
	4.00	0.5000	0.1592	0.5483	-0.0005	0.4450	0.0069
	4.50	0.5625	0.1790	0.7456	-0.0002	0.6110	0.0128
	5.00	0.6250	0.1989	0.9767	0.0037	0.8106	0.0247
0.250	1.00	0.2500	0.0796	0.1227	-0.0130	0.1133	-0.0119
	1.50	0.3750	0.1194	0.2562	-0.0067	0.2302	-0.0055
	2.00	0.5000	0.1592	0.4727	0.0025	0.4188	0.0028
	2.50	0.6250	0.1989	0.8562	0.0081	0.7373	0.0154
	2.75	0.6875	0.2188	1.1478	-0.0044	0.9637	0.0209
	3.00	0.7500	0.2387	1.4779	-0.0358	1.2845	0.0152
	3.25	0.8125	0.2586	1.7355	-0.0231	1.5945	0.0007
	3.50	0.8750	0.2785	2.0784	-0.0013	1.8598	0.0145
	3.75	0.9375	0.2984	2.4421	0.0001	2.1615	0.0242
	4.00	1.0000	0.3183	2.8116	-0.0022	2.4460	0.0277
	4.25	1.0625	0.3382	4.5627	0.2172	3.9702	0.2560
	4.50	1.1250	0.3581	5.6047	0.2394	4.9250	0.2902
	5.00	1.2500	0.3979	8.2578	0.3066	7.3244	0.3799
0.500	1.00	0.5000	0.1592	0.5568	-0.0001	0.5176	0.0013
	1.25	0.6250	0.1989	0.8026	0.0098	0.7474	0.0087
	1.50	0.7500	0.2387	1.1514	0.0150	1.0760	0.0161
	1.75	0.8750	0.2785	1.6232	0.0206	1.5327	0.0262
	2.00	1.000	0.3183	2.2286	0.0272	2.1429	0.0394
	2.25	1.1250	0.3581	2.9707	0.0372	2.9324	0.0559
	2.50	1.2500	0.3979	3.7690	0.0510	3.7722	0.0817
	3.00	1.5000	0.4775	8.3034	0.2010	7.4881	0.2801

Table 4.1: Mean power and thrust coefficients values of the simulated cases.

In Figures 4.1 and 4.2, the variation of the mean power and thrust coefficients with the reduced frequency is presented. Overall, the mean power coefficient graph shows that it increases monotonically with the reduced frequency, while on the other hand, the mean thrust coefficient shows a similar trend for some h values, but displays an interval where the mean coefficient value drops, exhibiting a bucket shape, for h = 0.250.

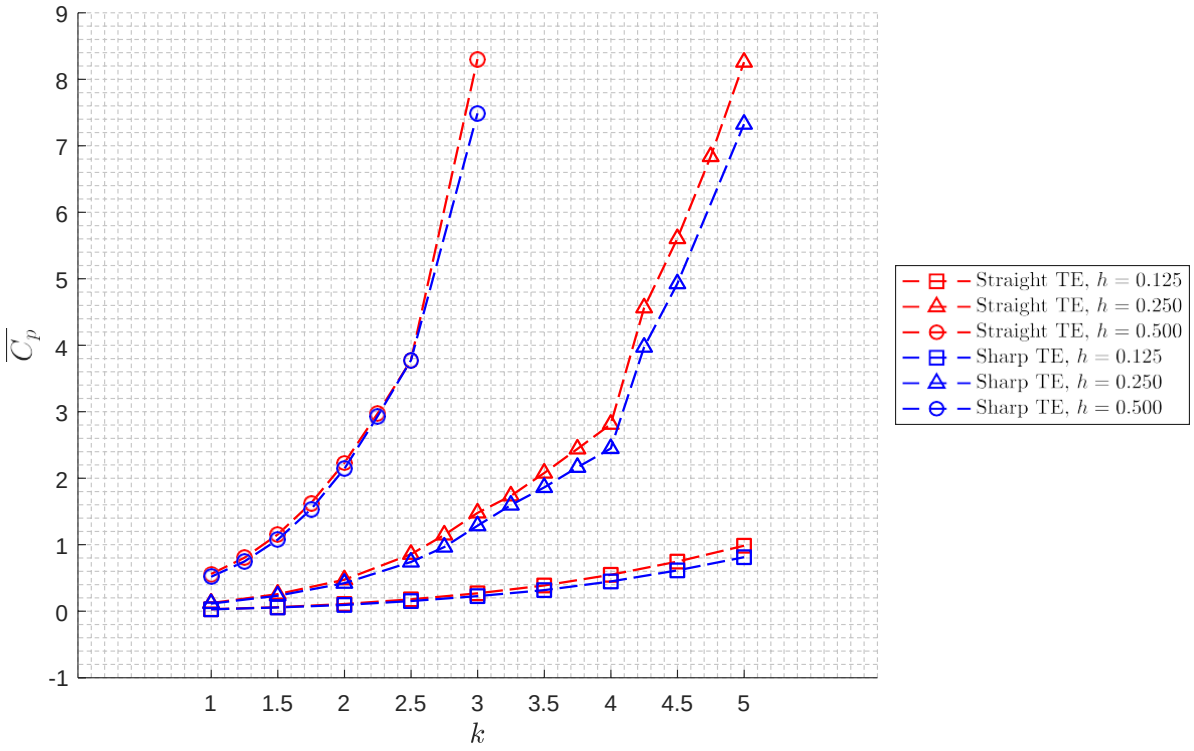

Figure 4.1: Variation of the mean power coefficient, $\overline{C_P}$, with the reduced frequency, k, and the nondimensional amplitude, h.

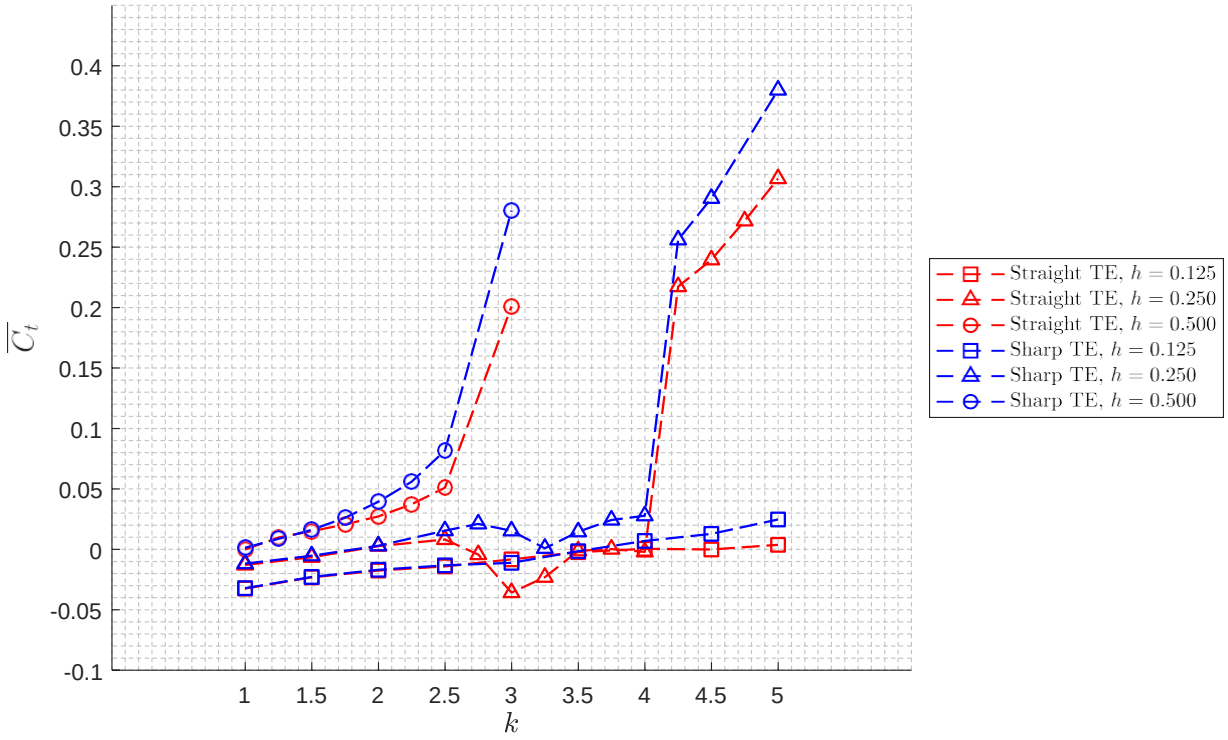

Figure 4.2: Variation of the mean thrust coefficient, $\overline{C_t}$, with the reduced frequency, k, and the nondimensional amplitude, h.

4.1 Influence of the Nondimensional Amplitude, *h*

The mean power coefficient presents similar behaviors for the various nondimensional amplitude values simulated, differing in the rate at which this behavior evolves with the reduced frequency. With the h increment, the $\overline{C_P}$ increases at a faster rate with k, due to instantaneous lift caused by the higher velocity resulting from bigger plunging amplitudes.

For the simulated nondimensional amplitude domain, the mean power coefficient displays a similar behavior for both plates, presenting slightly lower values for the flat plate with a straight trailing edge when compared to the flat plate with a sharp trailing edge, although still very close.

The mean thrust coefficient behaves similarly to the mean power coefficient, except for k values from 2.5 to 4.25. In this k range, the $\overline{C_t}$ does not display a continuous increment, presenting a sudden decrease. This phenomenon will be further investigated in section 4.3. Outside this range, the $\overline{C_t}$ value increases with the nondimensional amplitude, for each reduced frequency value, being this increment greater with the k increment.

4.2 Influence of the Reduced Frequency, *k*

Starting at the lowest value of k (k = 1.0), the mean power coefficient presents a similar behavior for all h values. As displayed in Equation (4.2), the coefficient progressively increases with both instantaneous lift and oscillating velocity, since in this case these two variables follow an oscillatory behavior with no considerable lag between them. As one of the parameters that describe this motion, the reduced frequency is related to the lift coefficient and velocity of the flat plate, and hence, to the power coefficient. When increasing k, the $\overline{C_p}$ also increases, as previously displayed in Figure 4.1.

However, contrarily to the other studied h values, the coefficient presents a slightly different behavior for a nondimensional amplitude of 0.250. For a reduced frequency between 4.0 and 4.25, the raise becomes more steep compared to the rest of the studied k domain.

Similar to the mean power coefficient, the mean thrust coefficient displays an almost identical behavior for both plates, presenting slightly lower values for the flat plate with a straight trailing edge over the flat plate with a sharp trailing edge, due to its susceptibility to pressure drag.

The mean thrust coefficient presents a similar behavior as the mean power coefficient, for the nondimensional amplitudes of 0.125 and 0.500. For these h values, the mean thrust coefficient progressively increases with the reduced frequency, being this increment rate enhanced as the k value raises.

However, for h = 0.250, the mean thrust coefficient varies differently. Despite starting sim-

ilarly, at values of k close to 2.5, both plates suffer a sudden decrease in the mean thrust coefficient. From that value, the mean thrust coefficient decreases for both plates as the reduced frequency increases, until reaching k = 3.0 and k = 3.25, for the flat plates with straight and sharp trailing-edges, respectively. Then, the $\overline{C_t}$ value starts increasing slowly until k = 4.0, where it suffers a drastic increase at this point. This steep increment is similar for both studied plates. Past this point, the mean coefficient keeps rising, in a continuous way, for the rest of the domain studied.

4.3 Analysis of the aerodynamic phenomena around k = 3.0

In summary, the mean thrust coefficient presents a segment of low values at k = 3.0 and its vicinity. Finding the root cause of this phenomenon passes by observing the pressure contour around the airfoil. For each plate, three different simulations were compared, corresponding to k values inside and outside the range where the $\overline{C_t}$ presents the previously referred bucket shape (k = 2.00, k = 3.00, and k = 4.25). Results show that a strong low-pressure zone appears near the trailing edge of the plates, highlighted in Figure 4.3.

Straight Trailing Edge | Sharp Trailing Edge

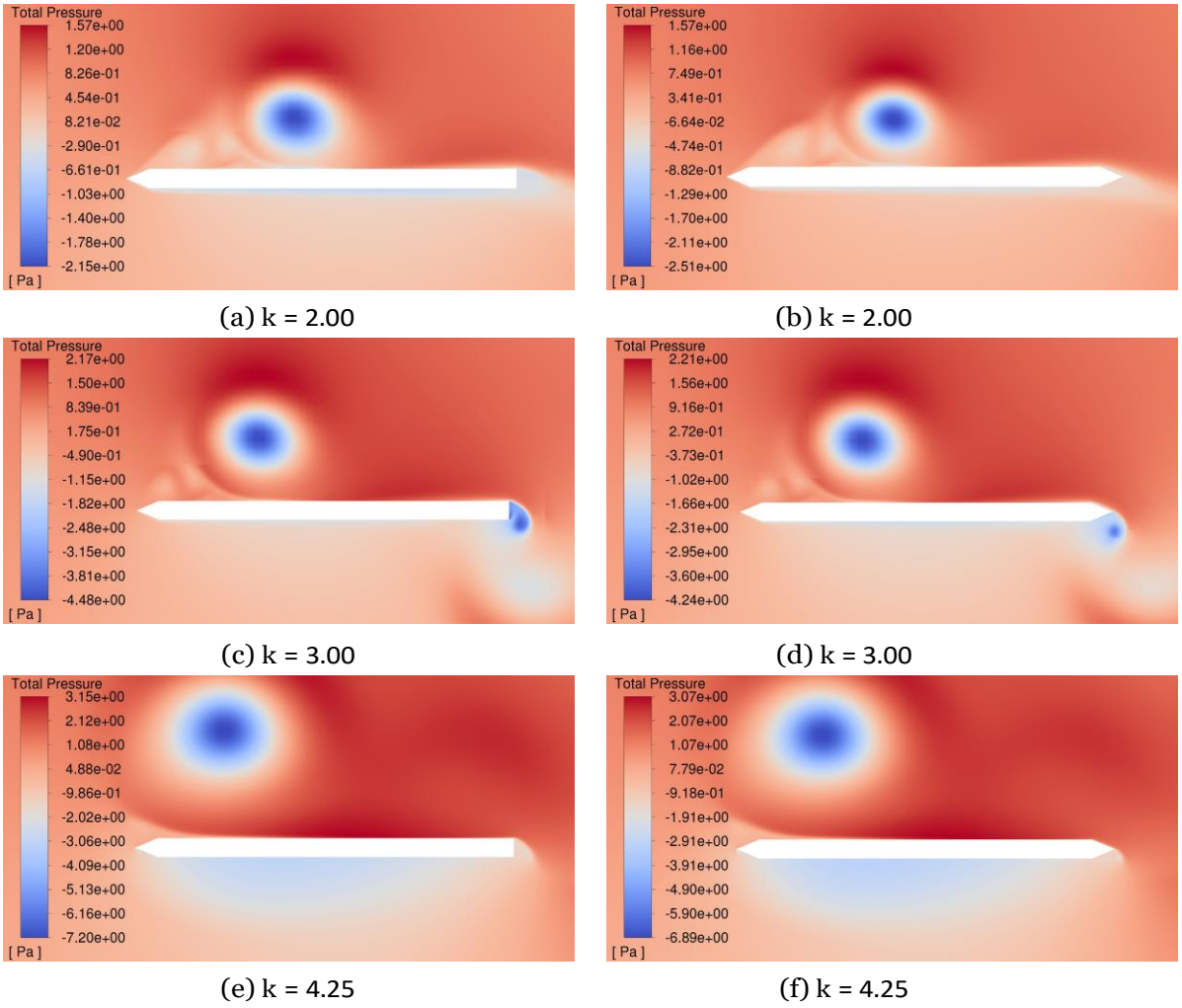

(a) k = 2.00 (b) k = 2.00

(c) k = 3.00 (d) k = 3.00

(e) k = 4.25 (f) k = 4.25

Figure 4.3: Low-pressure zone near the trailing edges of the flat plates at t/T = 0.50.

In some of the conditions, a stronger recirculation occurs at the trailing edge of the flat plates, creating a low-pressure zone that increases drag. The recirculation is visualized around t/T = 0.5 where the flat plates are at their lowest point of the trajectory. The obtained results suggest that the recirculation results from the interaction between the flat plate and the flow that suffered a vertical displacement due to the presence of the LEV and the previous down-wash motion of the plate. The sudden drag increase is justified by the suction effect created by the local low pressure, thus, resulting in a lower thrust coefficient.

The impact of the low-pressure zone is more noticeable in the flat plate with the straight trailing edge. The geometry of this plate creates a bigger separation of the flow in that area, resulting in greater drag. On the other hand, the geometry of the sharp trailing edge results in a less intense low-pressure zone than the one occurring with the first plate, but still not mitigating the phenomenon.

The values of the mean power coefficient did not present any noticeable variation due to this phenomenon since the pressure distribution at the trailing edge does not contribute to the resulting vertical forces, which influence the required power.

Furthermore, the power and thrust coefficients were analyzed over one period of the motion to understand the influence of the low-pressure zone, as displayed in Figure 4.4 and Figure 4.5.

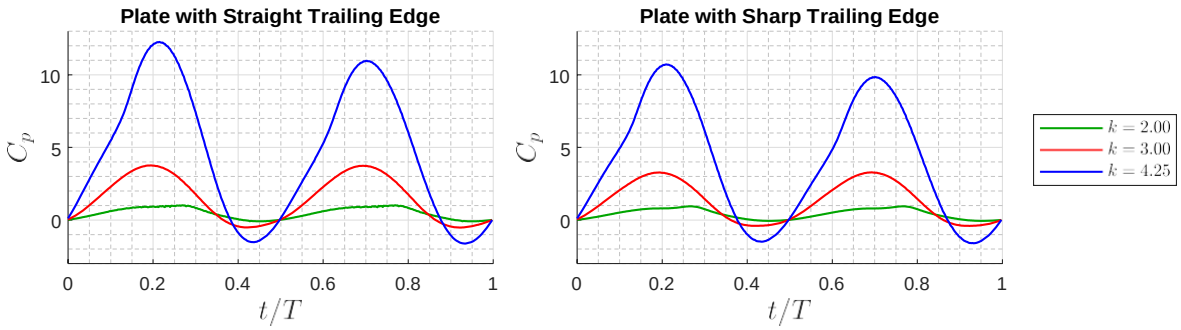

Figure 4.4: Power coefficient evolution throughout a period at different *k* values.

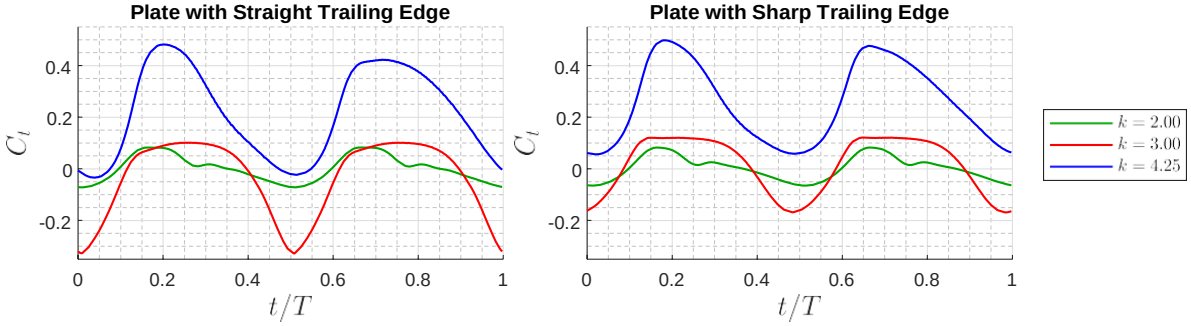

Figure 4.5: Thrust coefficient evolution throughout a period at different *k* values.

The power coefficient presented the expected behavior, increasing with the reduced frequency, which for a constant motion amplitude increases the speed of the plunging motion. As displayed in Figure 4.4, this coefficient reaches its maximum value around t/T = 0.25 and t/T = 0.75, which correspond to the instants of maximum velocity.

On the other hand, by comparing the pressure contours displayed in Figure 4.3 with the graphs above, an enormous impact is evidenced on the thrust coefficient. For k = 3.0, where the recirculation is visualized, there is a noticeable decrease of the thrust coefficient, being more pronounced when the airfoil has no vertical velocity. At those moments (t/T = 0.50 and t/T = 1.00), the C_t reduction is justified by the small separation zone that originates from the downwash created by the airfoil motion. However, this recirculation is not present during the entire movement, indicating that another phenomenon is responsible for the decrease of this coefficient during the remaining period.

The thrust created by a flat plate undergoing a pure plunging motion with an angle of attack of 0° is generated by aerodynamic phenomena occurring near the leading edge of the plate. Therefore, an analysis of the LEV's evolution with the reduced frequency was made in an attempt to identify the cause of the C_t reduction. Since the size of the LEV is an indicator of its strength, the distance between its center and the surface of the flat plate, y_v, normalized by the plate chord was used as a parameter for this investigation. As displayed in Figure 4.6, this parameter is presented as a function of the reduced frequency, at t/T = 0.25 that corresponds to the moment of the maximum velocity of the downward plunging motion, in an attempt to correlate it with the observed behavior of the performance parameters.

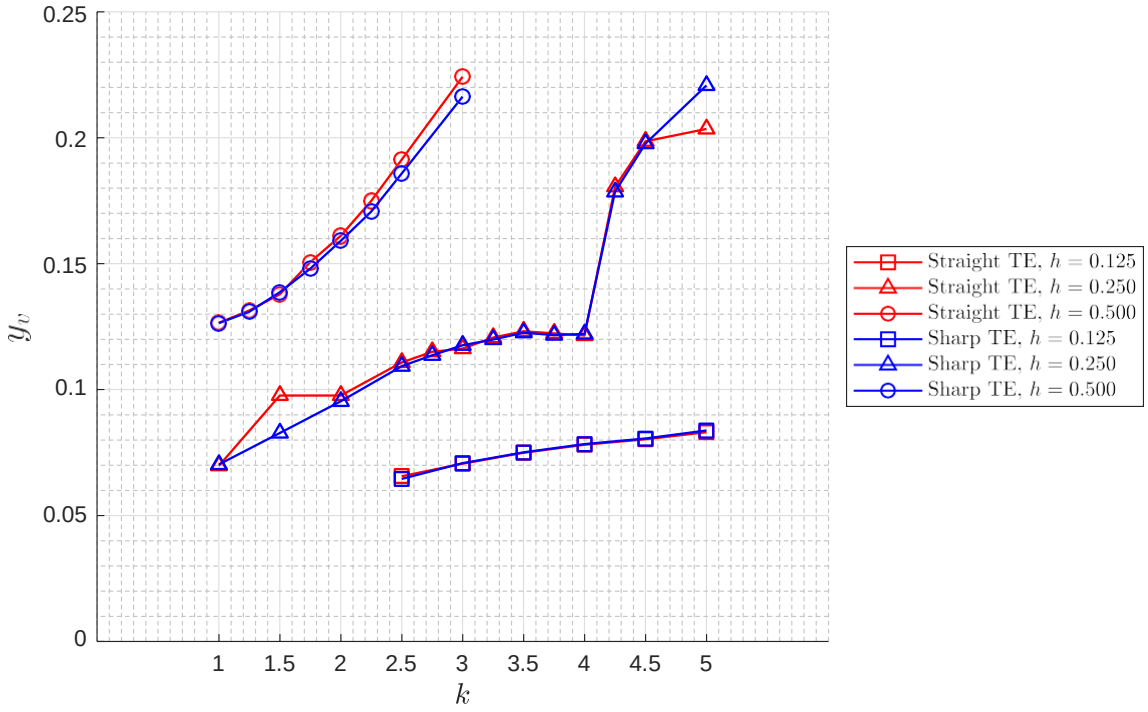

Figure 4.6: Variation of the normalized distance between the LEV's center and the plates' surface, y_v, with k.

This analysis is based on the leading edge and LEV of the plate, hence, both plates present an almost identical result since the shape of the trailing edge does not greatly influence the results.

For $h = 0.125$ and $h = 0.500$, the y_v value increases with k, presenting no fluctuation in the studied domain. However, for $h = 0.250$, the results vary differently, presenting a lower section for $2.5 \leq k \leq 4.25$. This reduced frequency range corresponds to the range in which the $\overline{C_t}$ presents the bucket shape. Furthermore, the y_v and the $\overline{C_t}$ lower sections present a comparable shape, with an almost constant value for the majority of the referred reduced frequency range but suddenly increasing from $k = 4.00$ to $k = 4.25$.

This similarity implies a correlation between the LEV's size and the $\overline{C_t}$ behavior observed. Nevertheless, the influence of the low-pressure zone near the trailing edge must not be undervalued.

4.4 Influence of the Strouhal Number, *St*

An attempt is made to understand the relation between the Strouhal number and the propulsive coefficients. As previously demonstrated in Equation (2.5), the Strouhal number can be represented in terms of the kh parameter. Thus, the mean power and thrust coefficients are presented in Figure 4.7 and Figure 4.8 as a function of kh.

As displayed in the graphs of the figures aforementioned, for kh values under 0.5, both the mean power and thrust coefficients present similar behaviors. In this range, cases with the same Strouhal numbers present almost identical mean power and thrust coefficients, independently of their kinematic parameters.

For kh values ranging between 0.5 and 1.0, the $\overline{C_p}$ and $\overline{C_t}$ parameters exhibit different tendencies. The mean power coefficient still presents a similar behavior, however lowering in precision with the increasing kh value. On the other hand, the mean thrust coefficient displays a larger variance due to the influence of the low-pressure zone located near the trailing edge and the LEV of the flat plates explained before.

At last, for kh values above 1.0, the simulated cases present a large range of $\overline{C_p}$ and $\overline{C_t}$ values for different conditions with similar Strouhal numbers. Above this kh value, as demonstrated by Jones et al. [20], the wake presents a nonsymmetric deflected pattern that can change from deflected up or down with rather small disturbances, which may justify this phenomenon.

For the entire kh range simulated, the flat plate with a sharp trailing edge presents a smaller variation of the mean thrust and power coefficients.

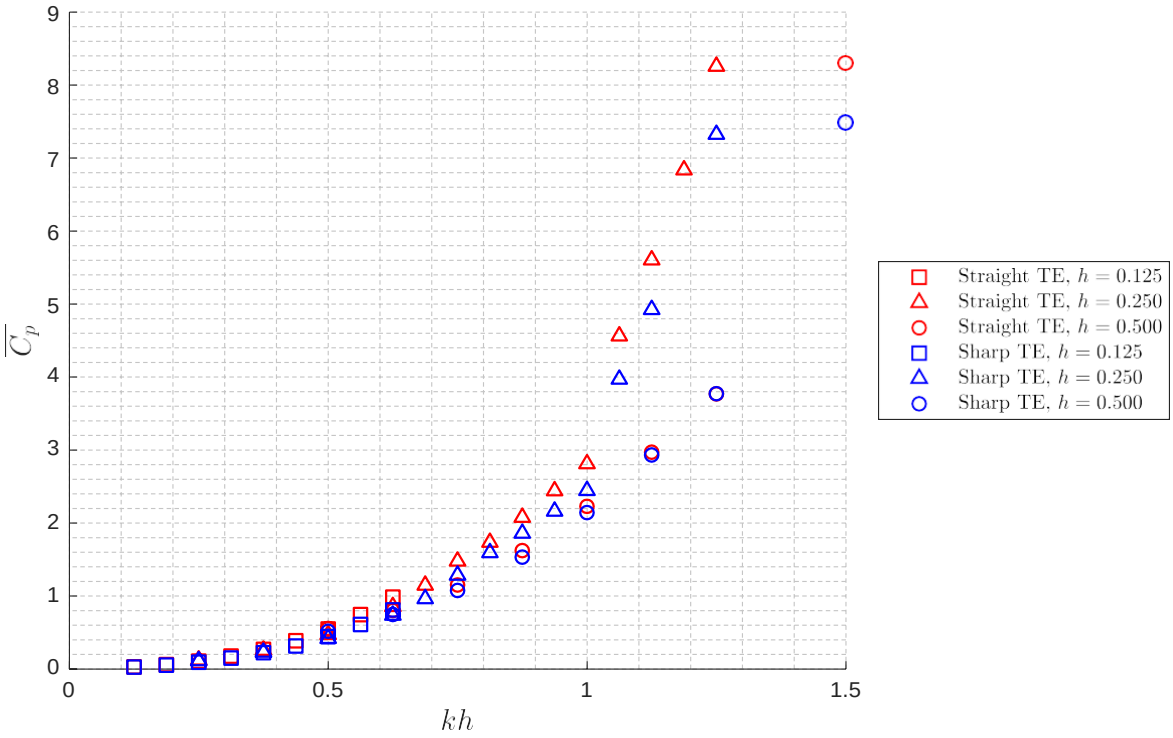

Figure 4.7: Variation of the mean power coefficient, $\overline{C_P}$, with kh.

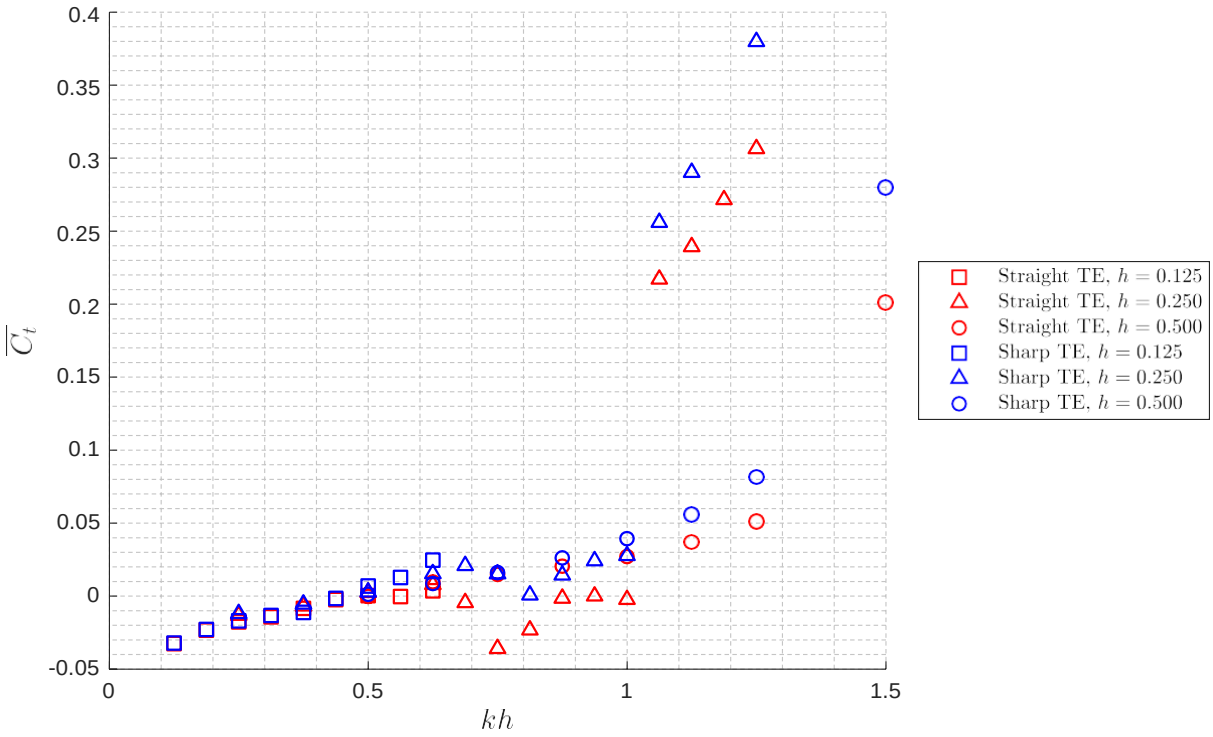

Figure 4.8: Variation of the mean thrust coefficient, $\overline{C_t}$, with kh.

Furthermore, Figure 4.3 suggests there might be a relation between the angles of detachment of the flow with the effective angle of attack. The relation between this parameter and the Strouhal number can be evidenced by rewriting Equation (2.7) as a function of k and h as

$$\alpha_{eff} = \arctan(-kh\sin(2\pi ft)) \tag{4.3}$$

which maximum value is given by

$$\alpha_{eff_{max}} = \arctan(kh) \tag{4.4}$$

In Figure 4.9, the $\alpha_{eff_{max}}$ is shown as a function of the reduced frequency for all the dimensionless amplitudes simulated.

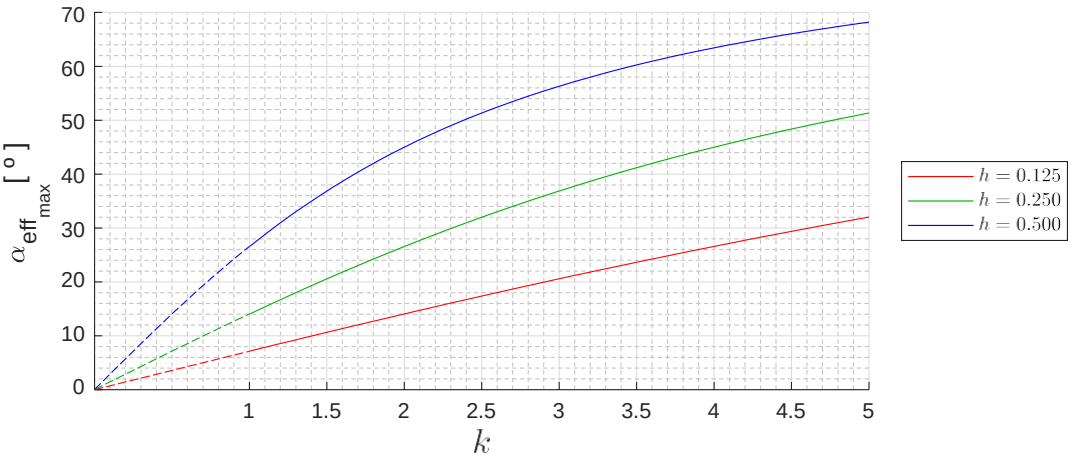

Figure 4.9: Maximum effective angle of attack evolution for different *k* values.

An attempt was made to correlate the maximum effective angle of attack with the formation of the recirculation near the trailing edge by comparing it with the angle of the detachment of the flow at the trailing edge. However, the obtained results did not display a correlation with the $\alpha_{eff_{max}}$, as supported by Gursul [50], who explains that this parameter is not an adequate indicator of the aerodynamic phenomena around the foil. This may be explained by the cinematic nature of Equation (4.4), since this equation is only dependent on the kinematic parameters k and h, which does not consider the likely influence of the LEV on the flow near the trailing edge, and thus, on the flow separation angle.

Chapter 5

Conclusion

The locomotion mechanisms present in nature have been a source of inspiration for the scientific community. These mechanisms are subjected to a continuous improvement based on evolution mechanisms, thus, they tend to offer an effective solution for their environmental conditions. Therefore, an interest in recreating them arises due to possible contributions in areas like military and civil with the development of small flying vehicles.

However, despite the urge to recreate these locomotion mechanisms and propulsive systems, a good understanding of the aerodynamic phenomena involved is first needed to allow the development of efficient vehicles and systems.

In this dissertation, two flat plates with different trailing-edge shapes (straight and sharp) undergoing a sinusoidal plunging motion are numerically analyzed. The Reynolds number is kept constant at $Re = 3.1 \times 10^3$, and the nondimensional amplitude and the reduced frequency investigated are between $0.125 \leq h \leq 0.500$ and $1.0 \leq k \leq 5.0$, respectively. Two performance parameters are selected to analyze the numerical results obtained: the mean power coefficient, $\overline{C_P}$, and the mean thrust coefficient, $\overline{C_t}$.

For the mean power coefficient, as the k value increase, the coefficient progressively increases, since both instantaneous lift and oscillating velocity increase with k, with no considerable lag between them. With the h increment, the $\overline{C_P}$ increases at a faster rate with k, due to velocity and resulting vertical forces from bigger plunging amplitudes. However, this coefficient presents a slightly different behavior for $h = 0.250$, displaying a more accentuated raise between 4.0 and 4.25 when compared to the rest of the studied k domain.

The mean thrust coefficient behaves similarly to the mean power coefficient for dimensionless amplitude values of 0.125 and 0.500. This coefficient increases with k, being the rate of change also greater as the reduced frequency increases. However, for $h = 0.250$, a different behavior is observed. In the cases with reduced frequency values roughly between $2.5 \leq k \leq 4.0$, a reduction of the mean thrust coefficient is seen. To understand this phenomenon, the pressure contours were analyzed around the airfoil, evidencing the presence of a low-pressure zone near the trailing edge that contributes to a drag surplus. Due to its position, this phenomenon has a considerable influence on the horizontal forces acting on the airfoil, while the average power coefficient is minimally influenced.

To better understand the influence of the low-pressure zone, the power and thrust coeffi-

cients were analyzed over one period of the motion. Results show that this coefficient reaches its maxes at the instants of maximum speed of the plate. For $k = 3.0$, there is an evident overall reduction of the thrust coefficient, being more accentuated when the airfoil has no vertical velocity ($t/T = 0.50$ and $t/T = 1.00$). Around this position, the phenomenon is justified by the recirculation near the trailing edge. However, this low-pressure zone is not present during the remaining motion, suggesting that another phenomenon is accountable for the C_t reduction.

The LEV's evolution was analyzed via the normalized distance between its center and the flat-plates' surface, which can be an indicator of the strength and position of the LEV. Results display similarities with the behavior observed for $\overline{C_t}$ with k, presenting no important fluctuation for $h = 0.125$ and $h = 0.500$, but presenting a lower section or $h = 0.250$ for a reduced frequency ranging between $k = 2.5$ and $k = 4.25$. This similarity suggests the influence of the LEV on the $\overline{C_t}$ phenomena observed.

By studying the Strouhal number in terms of kh, a predictable behavior of the performance parameters for the studied conditions is seen. The $\overline{C_P}$ parameter, for kh up to 1, different cases with equal St present almost an identical value, losing this feature past that value. On the other hand, for the $\overline{C_t}$ parameter, this predictability is observed up to $kh = 0.5$.

The trailing-edge shape has some weight on the performance parameters considered. As for the $\overline{C_P}$, the straight configuration displays slightly higher values in all simulated cases, when compared to the sharp one. The opposite occurs for the $\overline{C_t}$ whereas the straight configuration exhibits lower values when compared to the sharp one.

Even though the numerical simulations display the formation of that recirculation near the trailing edge and, hence, lower values of $\overline{C_t}$ for those conditions, further work is required to verify the phenomena. The low-pressure zone might be a result of the numerical model implemented and not correspond to the reality, due to the studied conditions, and can not be ignored.

The investigation of the unsteady aerodynamics of flat plates can offer great insights regarding propulsive systems since these simplified geometries remove some of the complexity from the analysis. Even though only plunging is considered, using pitching and/or surging actively or passively should also be considered since vortex shedding, when properly used will lead to improved future devices. Further investigation on the LEV's evolution is also needed to better predict the performance parameters and optimize the thrust and propulsive efficiency of the flapping mechanism.

Bibliography

[1] L. Petricca, P. Ohlckers, and C. Grinde, "Micro-and nano-air vehicles: State of the art," *International Journal of Aerospace Engineering*, vol. 2011, 2011.

[2] R. Shrestha, M. Benedict, V. Hrishikeshavan, and I. Chopra, "Hover performance of a small-scale helicopter rotor for flying on mars," *Journal of Aircraft*, vol. 53, no. 4, pp. 1160–1167, 2016.

[3] J. Winslow, H. Otsuka, B. Govindarajan, and I. Chopra, "Basic understanding of airfoil characteristics at low reynolds numbers (10^4–10^5)," *Journal of Aircraft*, vol. 55, no. 3, pp. 1050–1061, 2018.

[4] A. G. F. Marques, "Estudo experimental do movimento oscilatório vertical de uma placa plana: variação da espessura e da geometria do bordo de fuga," Master's thesis, 2020.

[5] X. Wu, X. Zhang, X. Tian, X. Li, and W. Lu, "A review on fluid dynamics of flapping foils," *Ocean Engineering*, vol. 195, 2020.

[6] R. Knoller and O. Verein, "Die gesetze des luftwiderstandes. verlag des osterreichischer flugtechnischen vereines," 1909.

[7] A. Betz, "Ein beitrag zur erklaerung segelfluges," *Z Flugtech Motorluftschiffahrt*, vol. 3, pp. 269–272, 1912.

[8] M. F. Platzer, K. D. Jones, J. Young, and J. C. Lai, "Flapping wing aerodynamics: progress and challenges," *AIAA Journal*, vol. 46, no. 9, pp. 2136–2149, 2008.

[9] I. Garrick *et al.*, "Propulsion of a flapping and oscillating airfoil," *NACA Report*, vol. 567, pp. 419–427, 1936.

[10] M. M. Koochesfahani, "Vortical patterns in the wake of an oscillating airfoil," *AIAA Journal*, vol. 27, no. 9, pp. 1200–1205, 1989.

[11] A. Andersen, T. Bohr, T. Schnipper, and J. H. Walther, "Wake structure and thrust generation of a flapping foil in two-dimensional flow," *J Fluid Mech*, vol. 812, 2017.

[12] J. M. Moubogha, U. Ehrenstein, and J. A. Astolfi, "Forces on a pitching plate: An experimental and numerical study," *Applied Ocean Research*, vol. 69, pp. 27–37, 2017.

[13] T. von Karman, "General aerodynamic theory-perfect fluids," *Aerodynamic Theory*, vol. 2, pp. 346–349, 1935.

[14] E. A. R. Camacho, "Numerical analysis of a plunging NACA0012 airfoil," Master's thesis, 2019.

[15] P. Freymuth, "Propulsive vortical signature of plunging and pitching airfoils," *AIAA Journal*, vol. 26, no. 7, pp. 881–883, 1988.

[16] J. Lai and M. Platzer, "Jet characteristics of a plunging airfoil," *AIAA Journal*, vol. 37, no. 12, pp. 1529–1537, 1999.

[17] G. C. Lewin and H. Haj-Hariri, "Modelling thrust generation of a two-dimensional heaving airfoil in a viscous flow," *Journal of Fluid Mechanics*, vol. 492, pp. 339–362, 2003.

[18] R. Godoy-Diana, J.-L. Aider, and J. E. Wesfreid, "Transitions in the wake of a flapping foil," *Physical Review E*, vol. 77, no. 1, 2008.

[19] J. Young and J. C. Lai, "Vortex lock-in phenomenon in the wake of a plunging airfoil," *AIAA Journal*, vol. 45, no. 2, pp. 485–490, 2007.

[20] K. Jones, C. Dohring, and M. Platzer, "Experimental and computational investigation of the Knoller-Betz effect," *AIAA Journal*, vol. 36, no. 7, pp. 1240–1246, 1998.

[21] G.-J. Li and X.-Y. Lu, "Force and power of flapping plates in a fluid," *Journal of Fluid Mechanics*, vol. 712, pp. 598–613, 2012.

[22] D. Rodrigues, E. A. Camacho, F. Neves, J. Barata, and A. R. Silva, "Plunging airfoil motion: Effects of unequal ascending and descending velocities," in *AIAA AVIATION 2020 FORUM*, 2020.

[23] G. C. Lewin and H. Haj-Hariri, "Modelling thrust generation of a two-dimensional heaving airfoil in a viscous flow," *Journal of Fluid Mechanics*, vol. 492, p. 339, 2003.

[24] K. B. Lua, T. Lim, K. Yeo, and G. Oo, "Wake-structure formation of a heaving two-dimensional elliptic airfoil," *AIAA Journal*, vol. 45, no. 7, pp. 1571–1583, 2007.

[25] Y. S. Baik, J. Rausch, L. Bernal, W. Shyy, and M. Ol, "Experimental study of governing parameters in pitching and plunging airfoil at low Reynolds number," in *48th AIAA aerospace sciences meeting including the new horizons forum and aerospace exposition*, 2010.

[26] A. Eslam Panah and J. Buchholz, "Vortex shedding and wake structure of a plunging wing," in *50th AIAA Aerospace Sciences Meeting including the New Horizons Forum and Aerospace Exposition*, 2012.

[27] A. E. Panah and J. H. Buchholz, "Parameter dependence of vortex interactions on a

two-dimensional plunging plate," *Experiments in Fluids*, vol. 55, no. 3, pp. 1–19, 2014.

[28] D. Kim, B. Strom, S. Mandre, and K. Breuer, "Energy harvesting performance and flow structure of an oscillating hydrofoil with finite span," *Journal of Fluids and Structures*, vol. 70, pp. 314–326, 2017.

[29] E. Camacho, F. Neves, A. Silva, and J. Barata, "Numerical investigation of frequency and amplitude influence on a plunging NACA0012," *Energies*, vol. 13, no. 8, 2020.

[30] E. A. Camacho, F. Neves, J. Barata, and A. R. Silva, "Plunging airfoil: Reynolds number and angle of attack effects," in *AIAA AVIATION 2020 FORUM*, 2020.

[31] C. P. Ellington, C. Van Den Berg, A. P. Willmott, and A. L. Thomas, "Leading-edge vortices in insect flight," *Nature*, vol. 384, no. 6610, pp. 626–630, 1996.

[32] H. Liu, C. P. Ellington, K. Kawachi, C. Van Den Berg, and A. P. Willmott, "A computational fluid dynamic study of hawkmoth hovering," *Journal of Experimental Biology*, vol. 201, no. 4, pp. 461–477, 1998.

[33] J. Pederzani and H. Haj-Hariri, "Numerical analysis of heaving flexible airfoils in a viscous flow," *AIAA Journal*, vol. 44, no. 11, pp. 2773–2779, 2006.

[34] S. Heathcote and I. Gursul, "Flexible flapping airfoil propulsion at low reynolds numbers," *AIAA Journal*, vol. 45, no. 5, pp. 1066–1079, 2007.

[35] W. Liu, Q. Xiao, and F. Cheng, "A bio-inspired study on tidal energy extraction with flexible flapping wings," *Bioinspiration & Biomimetics*, vol. 8, no. 3, 2013.

[36] P. A. Dewey, B. M. Boschitsch, K. W. Moored, H. A. Stone, and A. J. Smits, "Scaling laws for the thrust production of flexible pitching panels," *Journal of Fluid Mechanics*, vol. 732, pp. 29–46, 2013.

[37] G. S. Triantafyllou, M. Triantafyllou, and M. Grosenbaugh, "Optimal thrust development in oscillating foils with application to fish propulsion," *Journal of Fluids and Structures*, vol. 7, no. 2, pp. 205–224, 1993.

[38] K. Jones, M. Platzer, K. Jones, and M. Platzer, "Numerical computation of flapping-wing propulsion and power extraction," in *35th Aerospace Sciences Meeting and Exhibit*, 1997, p. 826.

[39] M. Yu, Z. Wang, and H. Hu, "Airfoil thickness effects on the thrust generation of plunging airfoils," *Journal of Aircraft*, vol. 49, no. 5, pp. 1434–1439, 2012.

[40] M. v. Yu, Z. Wang, and H. Hu, "High fidelity numerical simulation of airfoil thickness

and kinematics effects on flapping airfoil propulsion," *Journal of Fluids and Structures*, vol. 42, no. 5, pp. 166–186, 2013.

[41] K. D. Von Ellenrieder, K. Parker, and J. Soria, "Flow structures behind a heaving and pitching finite-span wing," *Journal of Fluid Mechanics*, vol. 490, pp. 129–138, 2003.

[42] S. Sarkar and K. Venkatraman, "Numerical simulation of incompressible viscous flow past a heaving airfoil," *International Journal for Numerical Methods in Fluids*, vol. 51, no. 1, pp. 1–29, 2005.

[43] W. Schmidt, "Der wellpropeller ein neuer antrieb fur wasser-land-und luftfahrzeuge," *Zeitschrift fur Flugwissenschaften*, vol. 13, no. 12, p. 472, 1965.

[44] I. H. Tuncer and M. F. Platzer, "Thrust generation due to airfoil flapping," *AIAA Journal*, vol. 34, no. 2, pp. 324–331, 1996.

[45] T. Kinsey and G. Dumas, "Optimal tandem configuration for oscillating-foils hydrokinetic turbine," *Journal of Fluids Engineering*, vol. 134, no. 3, 2012.

[46] A. Ashraf, J. Young, J. Lai, and M. Platzer, "Aerodynamic analysis of flapping-wing propellers for HALE aircraft," in *47th AIAA Aerospace Sciences Meeting including The New Horizons Forum and Aerospace Exposition*, 2009.

[47] *ANSYS®Fluent Theory Guide (Release 2021 R2)*, Ansys, Inc., 2021.

[48] F. R. Menter, "Two-equation eddy-viscosity turbulence models for engineering applications," *AIAA Journal*, vol. 32, no. 8, pp. 1598–1605, 1994.

[49] J. Bredberg, "On the wall boundary condition for turbulence models," *Chalmers University of Technology, Department of Thermo and Fluid Dynamics. Internal Report 00/4. G oteborg*, pp. 8–16, 2000.

[50] I. Gursul and D. Cleaver, "Plunging oscillations of airfoils and wings: Progress, opportunities, and challenges," *AIAA Journal*, vol. 57, no. 9, pp. 3648–3665, 2019.